

CHEM 26700 (Experimental Physical Chemistry) Lab Reports

Steven Labalme

March 4, 2023

Contents

1	UV-VIS ANALYSIS OF IODINE	1
2	TITLE	5
3	UV-VIS ANALYSIS OF IODINE	10
4	NMR ANALYSIS OF HEXYLAMINE	19
5	GCMS ANALYSIS OF BENZENE IN GASOLINE	25
6	ANALYSIS OF THE ELECTROCATALYTIC ACTIVITY OF PLATINUM, TIN, AND TITANIUM TOWARD THE HYDROGEN EVOLUTION REACTION	31

List of Figures

1	The absorption spectrum of gaseous I ₂ between $\lambda = 5000 - 6500 \text{ \AA}$	1
2	Birge-Sponer plot for the B state.	3
3	Morse potential curves.	3
1	Infrared absorption spectrum of air (background spectrum).	5
2	The five primary vibrational bands in a sample of air.	5
3	Rovibrational absorption spectrum of HCl.	6
4	Fitting data on the rovibrational transition wavenumbers $\bar{\nu}$ of HCl vs. a parameter m related to the rotational energy level from which such a rovibrational transition begins.	7
5	Morse potential curve.	8
1	The absorption spectrum of gaseous I ₂ between $\lambda = 5000 - 6500 \text{ \AA}$	12
2	Birge-Sponer plot for the B state.	14
3	Morse potential curves.	15
4	The absorption spectrum (in terms of the directly proportional molar extinction coefficient) of gaseous ⁵ (blue) and chloroform-based (orange) I ₂ between $\lambda = 300 - 800 \text{ nm}$	16
1	¹ H NMR spectrum of hexylamine. The protons on nitrogen exchange rapidly in solution, so since chemical exchanges cause spin decoupling, the A peak is a singlet.	19
2	¹³ C NMR spectrum of hexylamine. Notice that carbon 1 is the most downshifted because it's closest to the electronegative nitrogen atom.	20
3	A selection of inversion recovery ¹³ C NMR spectra for different delay times τ	21
4	Determining the spin-lattice relaxation time T_1 and the magnetization M_0 at equilibrium via nonlinear regression.	22
5	Two-dimensional ¹ H- ¹³ C HSQC spectrum of hexylamine.	23
1	Total ion chromatogram of diluted 87-gasoline in pentane.	25
2	Extracted ion chromatograms and extracted mass spectra for benzene and toluene.	26
3	Standard addition of benzene.	27
4	Extracted ion chromatogram of ethylbenzene.	28
5	Extracted mass spectra of ethylbenzene.	28
6	Extracted ion chromatogram of mesitylene.	29
7	Extracted mass spectra of mesitylene.	29
1	Experimental setup of the electrochemical cell. The three electrodes (working, reference, and counter) can be seen as well as the container in which the reaction took place. Not immediately pictured is the nitrogen needle used for pre-reaction sparging.	34
2	Extensive cyclic voltammogram exhibiting the HER over a Pt electrode in 0.1 M H ₂ SO ₄ . The current (in mA) flowing through the working electrode was measured against the applied potential (in V) as the potential ranged from 0.65 V to -0.15 V vs SHE and back again at a scan rate of 100 mV/s. A middle curve (Curve 4) was selected as representative and plotted in Excel. The HER begins at an overpotential of 0.02 V vs SHE on the negative scan, and remaining hydrides are oxidized off of the electrode surface on the positive scan resulting in the peak between -0.1-0 V.	36
3	Extensive cyclic voltammogram exhibiting the HER over a Sn electrode in 0.1 M H ₂ SO ₄ . The current (in mA) flowing through the working electrode was measured against the applied potential (in V) as the potential ranged from 0.65 V to -1.15 V vs SHE and back again at a scan rate of 100 mV/s. A middle curve (Curve 4) was selected as representative and plotted in Excel. The HER begins at an overpotential of 0.9 V vs SHE on the negative scan. No apparent feature correlates with the oxidation of remaining hydrides off of the electrode surface on the positive scan.	37

- 10 Tafel plot for the HER over a Ti electrode in 0.1 M H₂SO₄. The potentials (in V) were selected on the basis of preceding cyclic voltammetry experiments to surround the foot of the catalytic wave in 25 mV intervals. The logarithmic current densities were calculated from the average current measured at each potential in the last 30 s of a 100 s cyclic amperometry experiment conducted at a given potential, and normalized using the platinum electrode surface area of 0.63 cm². Data analysis and linear regression was performed in Excel using the Solver function. A positive Tafel slope is observed: $m = 402 \text{ mV/dec}$ and $b = 608 \text{ mV}$ for a fit to $\eta = m \cdot \log(j) + b$.

45

List of Tables

1	Peaks and their corresponding transitions.	2
2	Calculated spectroscopic constants and their reported values.	3
1	Infrared-active vibrational modes in air molecules.	6
2	Calculated spectroscopic constants and their reported values.	7
3	Calculated energy constants and their reported values.	8
1	Peaks and their corresponding transitions.	13
2	Calculated spectroscopic constants and their reported values.	14
1	Standard errors for the above nonlinear regressions.	22
2	The spin-lattice relaxation time and correlation time for each carbon in hexylamine.	23
1	Concentration of benzene in gasoline.	27
2	Concentrations of additional aromatic molecules.	30

Steven Labalme
12 January 2023

26 January 2023

1 UV-VIS ANALYSIS OF IODINE

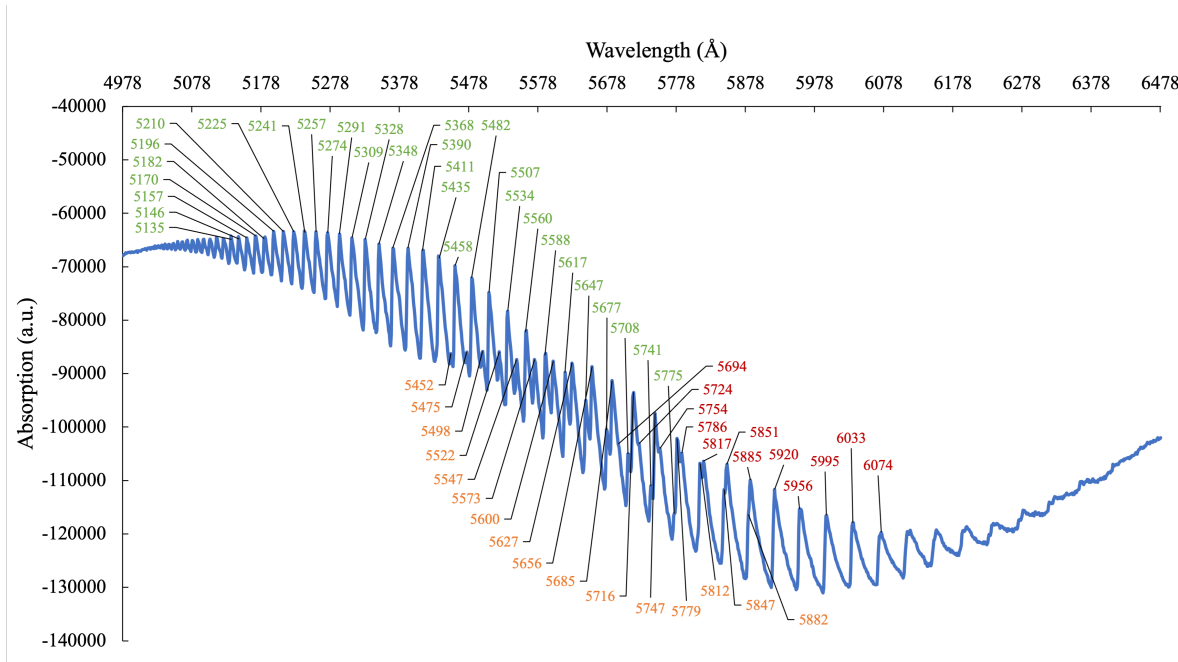


Figure 1: The absorption spectrum of gaseous I₂ between $\lambda = 5000 - 6500 \text{ \AA}$.

v'	v''	ω (cm $^{-1}$)	v'	v''	ω (cm $^{-1}$)	v'	v''	ω (cm $^{-1}$)
						10	2	16463
						11	2	16575
						12	2	16680
		13	1	17001		13	2	16789
14	0	17316	14	1	17102	14	2	16891
15	0	17418	15	1	17205	15	2	16992
16	0	17519	16	1	17304	16	2	17091
17	0	17614	17	1	17400	17	2	17190
18	0	17708	18	1	17494	18	2	17283
19	0	17803	19	1	17590	19	2	17379
20	0	17895	20	1	17680	20	2	17470
21	0	17985	21	1	17771	21	2	17562
22	0	18070	22	1	17857			
23	0	18158	23	1	17943			
24	0	18241	24	1	18027			
25	0	18321	25	1	18109			
26	0	18399	26	1	18188			
27	0	18480	27	1	18264			
28	0	18552	28	1	18341			
29	0	18628						
30	0	18698						
31	0	18768						
32	0	18835						
33	0	18900						
34	0	18960						
35	0	19022						
36	0	19080						
37	0	19138						
38	0	19193						
39	0	19245						
40	0	19297						
41	0	19342						
42	0	19391						
43	0	19432						
44	0	19474						

Table 1: Peaks and their corresponding transitions.

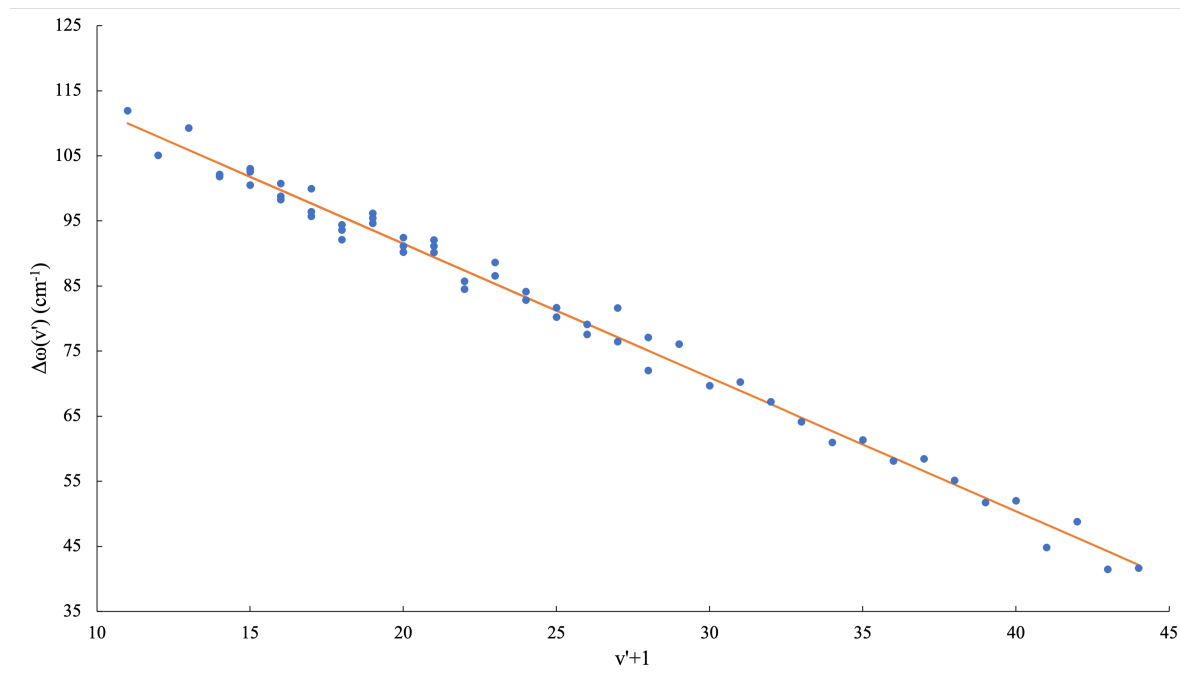


Figure 2: Birge-Sponer plot for the B state.

	$\bar{\nu}'_e$	$\bar{\nu}'_e x'_e$	D'_e	D'_0	$\bar{\nu}''_e$	$\bar{\nu}''_e x''_e$	D''_e	D''_0	T_e
Calculated values	132.62	1.0279	4277.2	4211.1	216.10	1.2583	9278.5	9170.7	12604
Literature values^{1,2}	125.69	0.764	4112	4046	214.50	0.614	12244	12137	15769.01

Table 2: Calculated spectroscopic constants and their reported values.

Note that the units for all values in Table 2 is cm^{-1} .

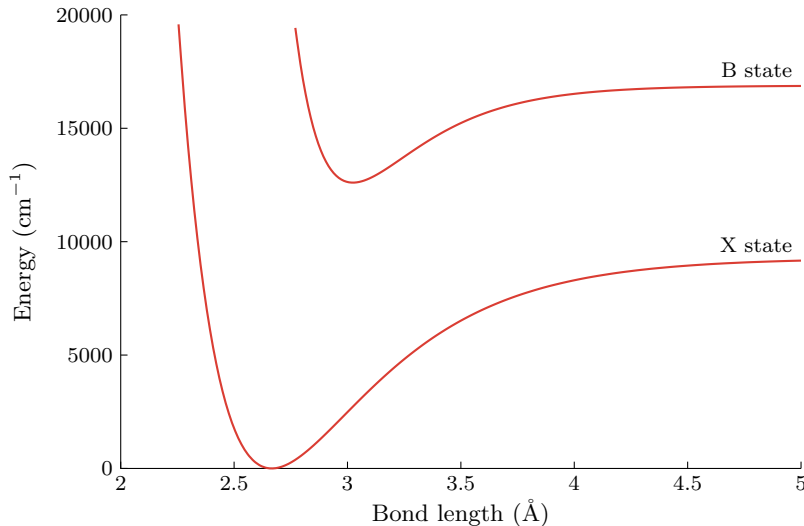


Figure 3: Morse potential curves.

References

- (1) Huber, K. P.; Herzberg, G. H. In *NIST Chemistry WebBook, NIST Standard Reference Database Number 69*, Linstrom, P. J., Mallard, W. G., Eds., <https://doi.org/10.18434/T4D303>; National Institute of Standards and Technology: Gaithersburg MD, 20899; Chapter Constants of Diatomic Molecules.
- (2) McNaught, I. J. The Electronic Spectrum of Iodine Revisited. *J. Chem. Educ.* **1980**, *57*, 101–105.
- (3) Lant, H. Electronic Spectroscopy: Absorption Spectra of Molecular Iodine in the Gas Phase, Rev. 1-21-23, 2023.
- (4) Verma, R. D. Ultraviolet Resonance Spectrum of the Iodine Molecule. *J. Chem. Phys.* **1960**, *32*, 738–749.
- (5) Saiz-Lopez, A.; Saunders, R. W.; Joseph, D. M.; Ashworth, S. H.; Plane, J. M. C. Absolute absorption cross-section and photolysis rate of I_2 . *Atmos. Chem. Phys.* **2004**, *4*, 1443–1450.
- (6) Seh, Z. W.; Kibsgaard, J.; Dickens, C. F.; Nørskov, J. C. J. K.; Jaramillo, T. F. Combining theory and experiment in electrocatalysis: Insights into materials design. *Science* **2017**, *355*, eaad4998.
- (7) Wuttig, A. Electrochemistry, Video lecture, Chicago, IL: University of Chicago, 2023.
- (8) Laursen, A. B.; Varela, A. S.; Dionigi, F.; Fanchiu, H.; Miller, C.; Trinhammer, O. L.; Rossmeisl, J.; Dahl, S. Electrochemical Hydrogen Evolution: Sabatier’s Principle and the Volcano Plot. *J. Chem. Educ.* **2012**, *89*, 1595–1599.
- (9) Wuttig, A.; Lant, H. Electrokinetics: Mechanism of Hydrogen Evolution on Catalytic Transition and Late Metal Electrodes, 2023.
- (10) Pourbaix, M., *Atlas of Electrochemical Equilibria in Aqueous Solutions*; National Association of Corrosion Engineers: 1440 South Creek Drive, Houston, Texas 77084, 1974.
- (11) Connor, P.; Schuch, J.; Kaiser, B.; Jaegermann, W. The Determination of Electrochemical Active Surface Area and Specific Capacity Revisited for the System MnO_x as an Oxygen Evolution Catalyst. *Z. Phys. Chem.* **2020**, *234*, 979–994.

Steven Labalme
26 January 2023

2 February 2023

2 TITLE

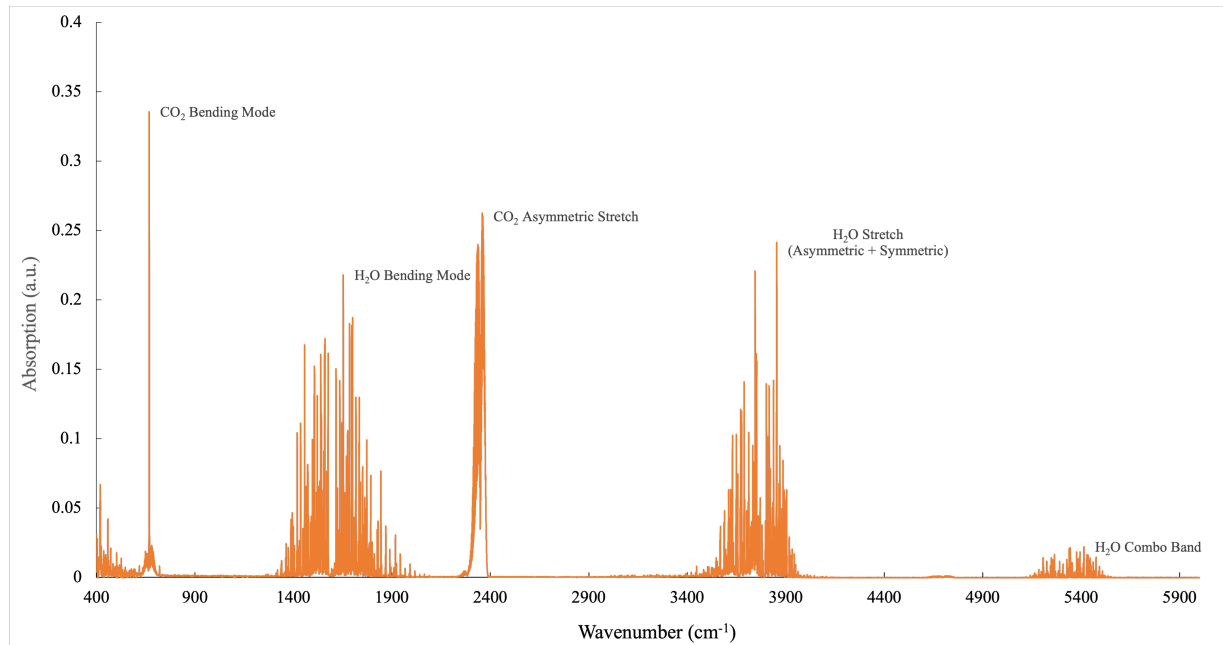


Figure 1: Infrared absorption spectrum of air (background spectrum).

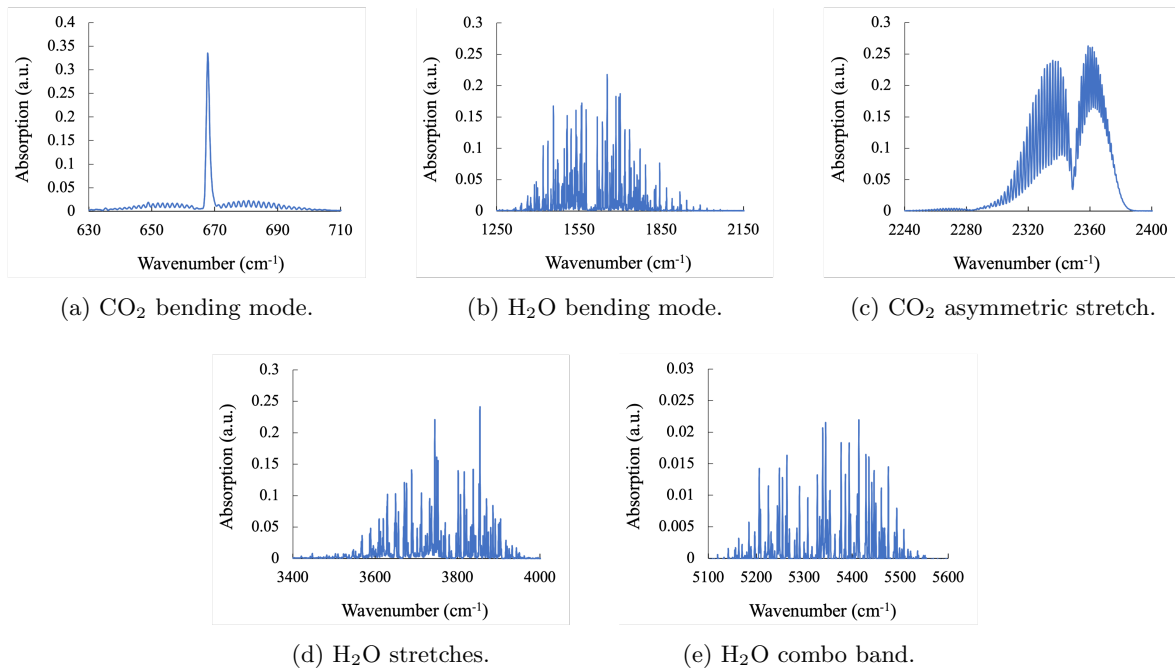


Figure 2: The five primary vibrational bands in a sample of air.

Wavenumber Range (cm^{-1})	Molecule	Vibrational Band
630-710	CO_2	Bending
1250-2150	H_2O	Bending
2240-2400	CO_2	Asymmetric stretch
3400-4000	H_2O	Asymmetric & symmetric stretch
5100-5600	H_2O	Combo band

Table 1: Infrared-active vibrational modes in air molecules.

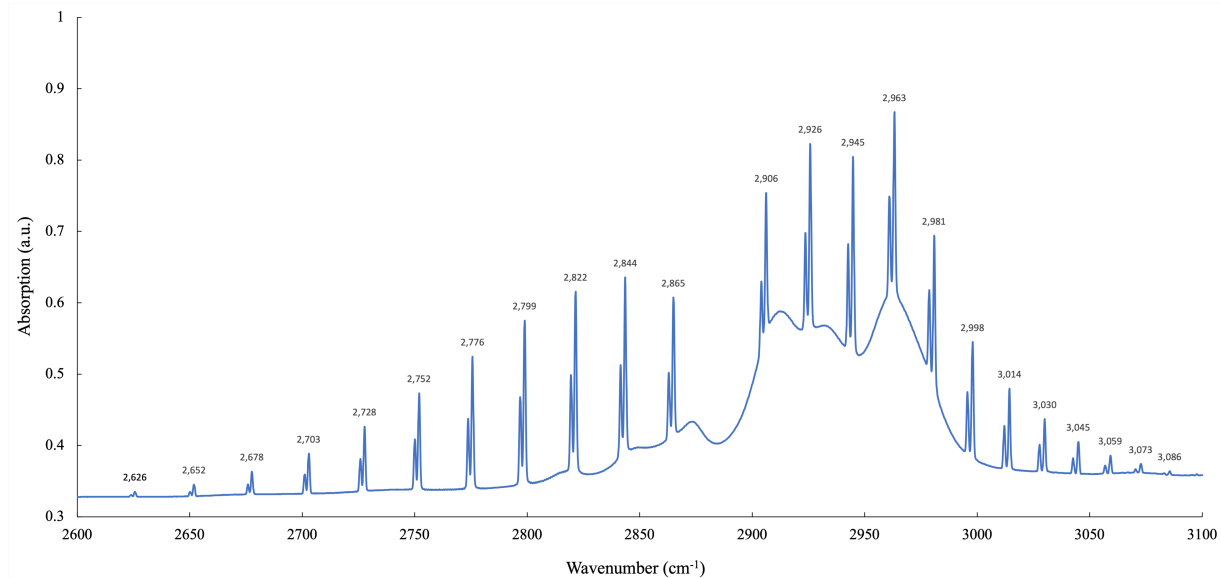


Figure 3: Rovibrational absorption spectrum of HCl.

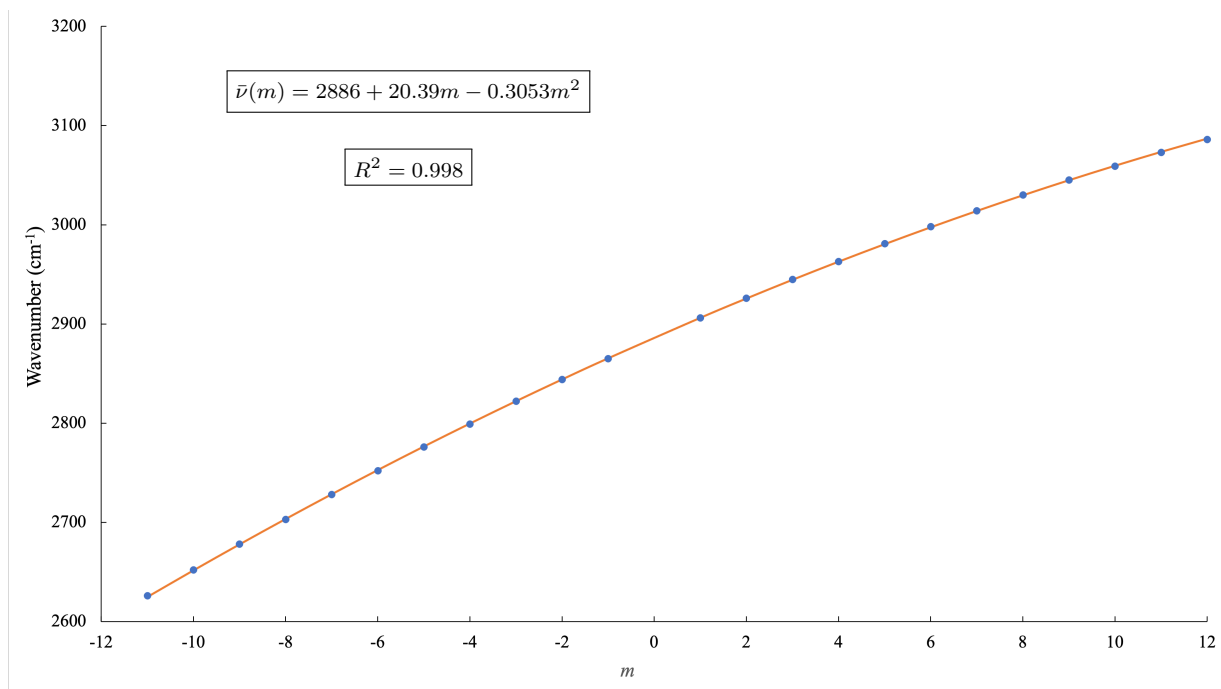


Figure 4: Fitting data on the rovibrational transition wavenumbers $\bar{\nu}$ of HCl vs. a parameter m related to the rotational energy level from which such a rovibrational transition begins.

	B_e (cm ⁻¹)	α_e (cm ⁻¹)	$\bar{\nu}_0$ (cm ⁻¹)
Calculated values	10.50	0.3053	2886
Literature values	10.59 ¹	0.3072 ¹	2991 ¹

Table 2: Calculated spectroscopic constants and their reported values.

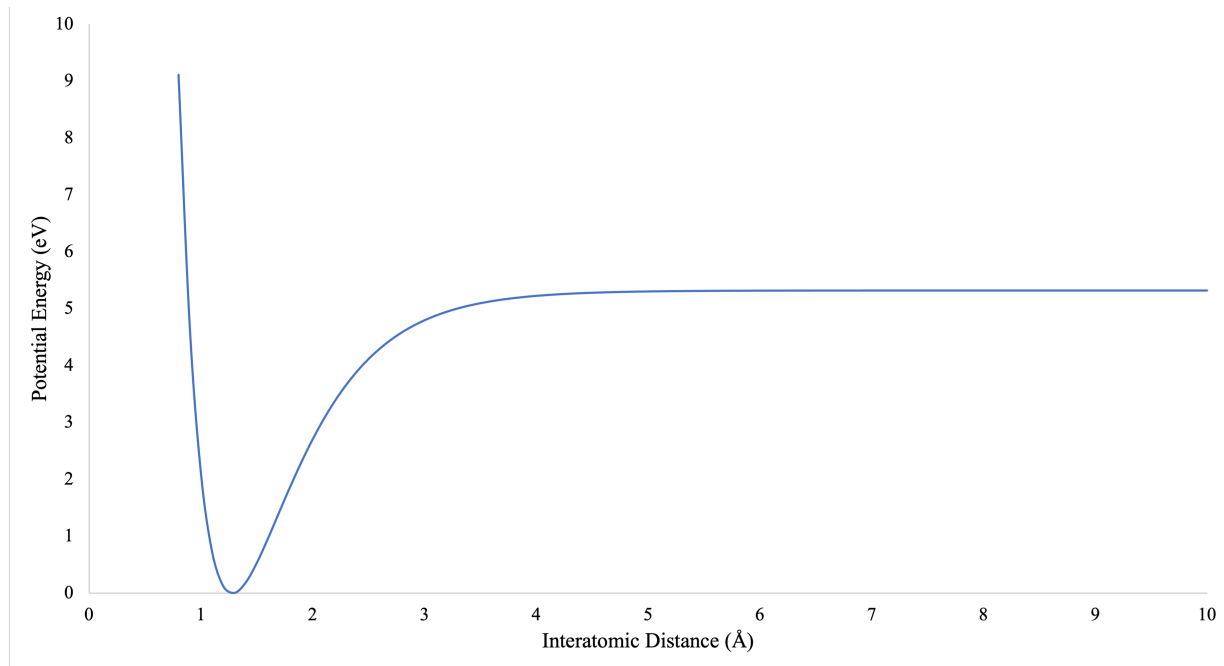


Figure 5: Morse potential curve.

	$\bar{\nu}_e$ (cm^{-1})	x_e	D_e (eV)	r_e (\AA)
Calculated values	2990	0.01741	5.320	1.281
Literature values	2991 ¹	0.01766 ¹	5.319 ¹	1.275 ¹

Table 3: Calculated energy constants and their reported values.

References

- (1) Huber, K. P.; Herzberg, G. H. In *NIST Chemistry WebBook, NIST Standard Reference Database Number 69*, Linstrom, P. J., Mallard, W. G., Eds., <https://doi.org/10.18434/T4D303>; National Institute of Standards and Technology: Gaithersburg MD, 20899; Chapter Constants of Diatomic Molecules.
- (2) McNaught, I. J. The Electronic Spectrum of Iodine Revisited. *J. Chem. Educ.* **1980**, *57*, 101–105.
- (3) Lant, H. Electronic Spectroscopy: Absorption Spectra of Molecular Iodine in the Gas Phase, Rev. 1-21-23, 2023.
- (4) Verma, R. D. Ultraviolet Resonance Spectrum of the Iodine Molecule. *J. Chem. Phys.* **1960**, *32*, 738–749.
- (5) Saiz-Lopez, A.; Saunders, R. W.; Joseph, D. M.; Ashworth, S. H.; Plane, J. M. C. Absolute absorption cross-section and photolysis rate of I_2 . *Atmos. Chem. Phys.* **2004**, *4*, 1443–1450.
- (6) Seh, Z. W.; Kibsgaard, J.; Dickens, C. F.; Nørskov, J. C. J. K.; Jaramillo, T. F. Combining theory and experiment in electrocatalysis: Insights into materials design. *Science* **2017**, *355*, eaad4998.
- (7) Wuttig, A. Electrochemistry, Video lecture, Chicago, IL: University of Chicago, 2023.
- (8) Laursen, A. B.; Varela, A. S.; Dionigi, F.; Fanchiu, H.; Miller, C.; Trinhammer, O. L.; Rossmeisl, J.; Dahl, S. Electrochemical Hydrogen Evolution: Sabatier’s Principle and the Volcano Plot. *J. Chem. Educ.* **2012**, *89*, 1595–1599.
- (9) Wuttig, A.; Lant, H. Electrokinetics: Mechanism of Hydrogen Evolution on Catalytic Transition and Late Metal Electrodes, 2023.
- (10) Pourbaix, M., *Atlas of Electrochemical Equilibria in Aqueous Solutions*; National Association of Corrosion Engineers: 1440 South Creek Drive, Houston, Texas 77084, 1974.
- (11) Connor, P.; Schuch, J.; Kaiser, B.; Jaegermann, W. The Determination of Electrochemical Active Surface Area and Specific Capacity Revisited for the System MnO_x as an Oxygen Evolution Catalyst. *Z. Phys. Chem.* **2020**, *234*, 979–994.

Steven Labalme
TA: Rowan Simonet
Lab partners: Eric Yuan and Kate Kaplin
12 January 2023

10 February 2023

3 UV-VIS ANALYSIS OF IODINE

Abstract

The goal of this experiment is to determine several spectroscopic constants of iodine and use them to calculate the potential energy surface, approximated as a Morse potential, of the ground and second excited states. Additionally, it is desired to compare solution-phase and gas-phase data to obtain insight into how phase changes alter molecular dynamics.

As a result of both gas- and solution-phase analyses, the fundamental vibrational frequency, first anharmonicity constant, well depth, dissociation energy (from the zero point energy), difference in energy between the X and B states, and Morse constant β were calculated.

The aim is to provide an experimental verification of the basic quantum mechanical theory of molecular transition mechanics.

Introduction

The experiment described herein has two main parts. The primary purpose of the first of these is to determine several spectroscopic constants of diatomic iodine (I_2) from the gas-phase ultraviolet-visible (UV-Vis) absorption spectrum and use them to calculate the potential energy surface, approximated as a Morse potential, of the ground ($^1\Sigma_g^+$) and second excited ($^3\Pi_{\text{ou}}^+$) states^{3,2}. The primary purpose of the second of these is obtain a solution-phase UV-Vis absorption spectrum and, from it, calculate the molar extinction coefficient.

From the gas-phase data in particular, we can obtain the frequencies, anharmonicities, and magnitudes of each electronic state, the dissociation energies of each electronic state, and more, but we will only focus on the first two herein². From the solution-phase data, we can only obtain the frequency and magnitude of the transition.

As mentioned above, we will collect our data via UV-Vis spectroscopy (gas phase and solution phase). We will analyze anharmonicity (and its derived constants) using a linear model and hence linear regression. All theoretical calculations build up to the construction of a Morse potential.

The main theoretical idea behind the experiment is that incoming radiation couples to the eigenstates of the system. Specifically, frequencies of radiation that (nearly) exactly match the difference in energy between two quantum states are capable of causing a transition. In the UV-Vis range, this excitation occurs between vibronic energy levels. The electronic energy levels are represented by discrete potential energy surfaces (PES's), and the vibrational energy levels occur as sublevels within the larger electronic levels. If we approximate the electronic potential wells as parabolas (corresponding to a harmonically oscillating molecule), we can prove via quantum mechanics that the energies of the vibrational sublevels depend on an indexing parameter v via

$$E_v = \bar{\nu}_e \left(v + \frac{1}{2} \right)$$

where $\bar{\nu}_e$ is the fundamental vibrational frequency. Realizing that a harmonic oscillator is not a good approximation, we can introduce anharmonicity into the math by expanding the above energy levels as a power series in $v + 1/2$. Using this energy function to second order, we can derive a formula for the spacing between adjacent vibrational energy levels that is linear. This formula comes in two flavors, one for changes in the vibrational energy level to which an electron is excited and one for changes in the ground state vibrational energy level (i.e., fundamental transitions vs. hot bands). Both are listed below.

$$\Delta\bar{\nu}(v') = \bar{\nu}'_e - 2\bar{\nu}'_e x'_e (v' + 1)$$

$$\Delta\bar{\nu}(v'') = \bar{\nu}''_e - 2\bar{\nu}''_e x''_e (v'' + 1)$$

In the above equations, x_e is the first anharmonicity constant, and the other variables are as defined above.

Thus, fitting the peaks on a UV-Vis spectrum (which correspond to distinct vibronic transitions) allows us to reverse engineer the fundamental frequency and anharmonicity parameters. These parameters give information on the shape of the potential well that can be fit to a Morse potential via³

$$D_e \approx \frac{\bar{\nu}_e}{4x_e} \quad \beta = \bar{\nu}_e \pi \cdot \sqrt{\frac{2c\mu}{hD_e}}$$

In the above equations, $c = 2.998 \times 10^8 \text{ m s}^{-1}$ is the speed of light, $\mu = 1.06 \times 10^{-25} \text{ kg}$ is the reduced mass of I_2 , $h = 6.626 \times 10^{-34} \text{ Js}$ is Planck's constant, and all other variables are as defined above.

Per Verma [4], the Morse potential is an excellent approximation for the PES of I_2 , even among similar diatomics, so we can expect physically comparable results from the following equation even using such a crude experiment and theoretical model.

$$U(r) = D_e(e^{-\beta(r-r_e)} - 1)^2$$

In the above equation, U is the potential energy, r is the bond distance on which U depends, β is the Morse constant, r_e is the equilibrium constant, and e is Euler's number.

Experimental

To collect the gas-phase spectrum, an apparatus centered around a SPEX 500M monochromator was used. Said apparatus also included a light source, the I_2 sample, a light shutter, and an RCA 6217 photomultiplier tube (PMT) which functioned as a detector. Removal of external light was accomplished by carrying out the experiment in a darkened room and shrouding the PMT in an additional blanket. Data collection was performed in LabView from National Instruments³. During the post-collection analysis phase, extra care was taken at the lower ends of $(v', 0)$, $(v', 1)$, and $(v', 2)$ peaks since hot bands eventually outweigh other data. However, the hot bands were still analyzed as they actually make it possible to obtain much more data from the excited-state Birge-Sponer plot, and data at all for a ground-state Birge-Sponer plot².

To collect the solution-phase spectrum, an Ocean Optics USB4000 spectrometer was connected to a standard desktop computer running OceanView. The solvent used for I_2 was chloroform (CHCl_3). An extremely dilute sample was used to bring the data in to the Beer's Law region (to allow for calculation of the molar extinction coefficient, as previously mentioned). Beer's law is given by

$$A = \varepsilon bC$$

where A is absorbance, ε is the molar extinction coefficient, b is the path length (1 cm in this case since that's the width of the cuvette), and C is the concentration of the dilution ($2.8 \times 10^{-4} \text{ M}$ in this case).

The overall procedure was as follows. First, a broad-spectrum scan of the gas-phase sample was collected to identify the region of interest. Next, a narrow-range spectrum was collected to far greater accuracy, allowing for the resolution of vibrational transitions. A subsequent calibration step (using a mercury lamp that emits at one known characteristic wavelength) was performed to account for any error in the monochromator. For the solution, a chloroform and cuvette background, and a dark background were taken. Then, the sample was diluted using 0.7 mL of a 0.01 M stock solution and an additional 24.3 mL of pure chloroform; the result was a $2.8 \times 10^{-4} \text{ M}$ solution of I_2 in CHCl_3 . Lastly, a UV-Vis absorption spectrum of this sample was taken.

Safety goggles and nitrile gloves were used at all times when handling chloroform-containing samples.

Results

As determined by the initial broad-spectrum scan, the gas-phase spectrum was collected between 5000-6500 Å. It is plotted below in Figure 1. Note that the colored numbers correspond to the wavelengths of certain vibrational transitions (green for ground state, orange for the first hot band, red for the second hot band).

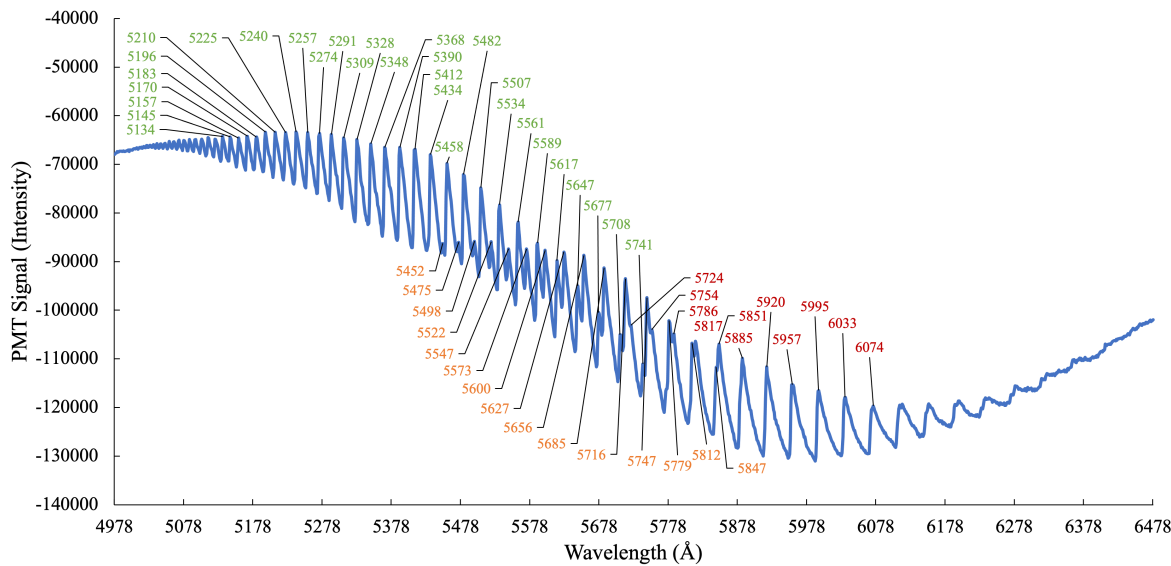


Figure 1: The absorption spectrum of gaseous I_2 between $\lambda = 5000 - 6500 \text{ \AA}$.

Since the PMT is not capable of measuring absorption directly and unforeseen circumstances prevented the collection of a background spectrum in a timely manner, the spectrum is plotted in *intensity* vs. wavelength instead of the standard *absorption* vs. wavelength. Support for an accurate measurement of the wavelength comes from the aforementioned mercury lamp calibration step, and steps have been taken to ensure that the PMT intensity (as described above) is also accurate.

The overall trend observed in Figure 1 is representative of the electronic absorption band, while the fine structure is vibrational in nature. The variable peak spacing is representative of anharmonicity and is characterized below in Figure 2.

First, though, the peaks labeled in Figure 1 are tabulated and assigned to vibronic transitions using known reference values. The result is as follows. Note that wavelength has been converted to wavenumber.

v'	v''	ω (cm $^{-1}$)	v'	v''	ω (cm $^{-1}$)	v'	v''	ω (cm $^{-1}$)
						10	2	16464
						11	2	16576
						12	2	16681
						13	2	16787
			14	1	17103	14	2	16892
15	0	17419	15	1	17206	15	2	16992
16	0	17519	16	1	17304	16	2	17091
17	0	17615	17	1	17400	17	2	17191
18	0	17709	18	1	17495	18	2	17283
19	0	17803	19	1	17590	19	2	17379
20	0	17892	20	1	17680	20	2	17470
21	0	17982	21	1	17771			
22	0	18070	22	1	17857			
23	0	18159	23	1	17944			
24	0	18242	24	1	18028			
25	0	18322	25	1	18109			
26	0	18402	26	1	18188			
27	0	18477	27	1	18265			
28	0	18553	28	1	18342			
29	0	18629						
30	0	18699						
31	0	18769						
32	0	18836						
33	0	18900						
34	0	18961						
35	0	19022						
36	0	19084						
37	0	19139						
38	0	19194						
39	0	19246						
40	0	19294						
41	0	19342						
42	0	19391						
43	0	19436						
44	0	19478						

Table 1: Peaks and their corresponding transitions.

Using the data in Table 1 and the $\Delta\bar{\nu}(v')$ equation from the introduction, it is possible to construct and characterize a Birge-Sponer plot (Figure 2) to determine both the fundamental vibration frequency and the first anharmonicity constant. All three data sets ($v'' = 0, 1, 2$) are plotted on top of each other, and are plotted versus the change in wavenumber.

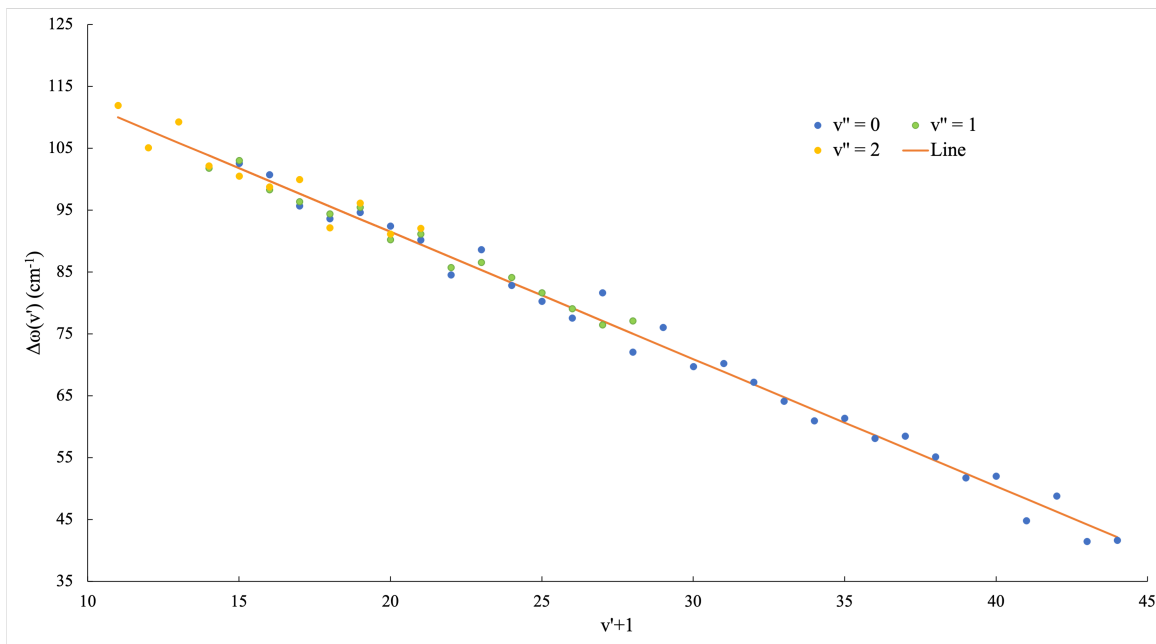


Figure 2: Birge-Sponer plot for the B state.

Evidently, the linear analysis provides a remarkable fit to the data, and it is not immediately obvious that a higher-order energy equation (e.g., cubic, quartic, etc.) would have been necessary to account for additional anharmonicity.

The above analysis was repeated for the $\Delta\nu(v'')$ data. From $\bar{\nu}'_e$, $\delta\nu'_e x'_e$, $\bar{\nu}''_e$, and $\delta\nu''_e x''_e$, the ground and excited state dissociation energies from both the bottom of the energy well and the zero point energy can be calculated: D'_e , D'_0 , D''_e , and D''_0 . The calculation of the energy gap between electronic levels T_e followed from the previous data and additional information on the hypothetical energy of a dissociated excited I₂ molecule. All constants are summarized below.

	$\bar{\nu}'_e$	$\bar{\nu}'_e x'_e$	D'_e	D'_0	$\bar{\nu}''_e$	$\bar{\nu}''_e x''_e$	D''_e	D''_0	T_e
Calculated values	132.22	1.019	4288.6	4222.7	214.97	0.912	12 672	12 564	15 986.11
Literature values	125.69 ¹	0.764 ¹	5169.3	5106.6	214.50 ¹	0.614 ¹	18 734	18 627	15 769.01 ¹

Table 2: Calculated spectroscopic constants and their reported values.

Note that the unit for all values in Table 2 is cm⁻¹. Also note that the D_e and D_0 values were calculated from the NIST $\bar{\nu}'_e$ and $x'_e = \bar{\nu}'_e x'_e / \bar{\nu}'_e$ values using Equations 9 and 12 in Lant [3], respectively.

The experimental values in Table 2 may be plugged into two Morse potential equations as follows. D_e values go in directly. β values must be calculated as in the introduction. Equilibrium bond length values are found in Lant [3]. And T_e gives the vertical offset between the two equations (the zero of energy was arbitrarily defined to be the bottom of the ground (X) state potential well).

Additionally, as wavenumbers have been used throughout the analysis, they are used as the unit of energy on the y-axis of Figure 3 below. Lastly, angstroms are a natural scale on which to discuss molecules, so bond length (the x-axis below) is given in terms of it. All above determinations of error suggest that the variables are being measured largely accurately.

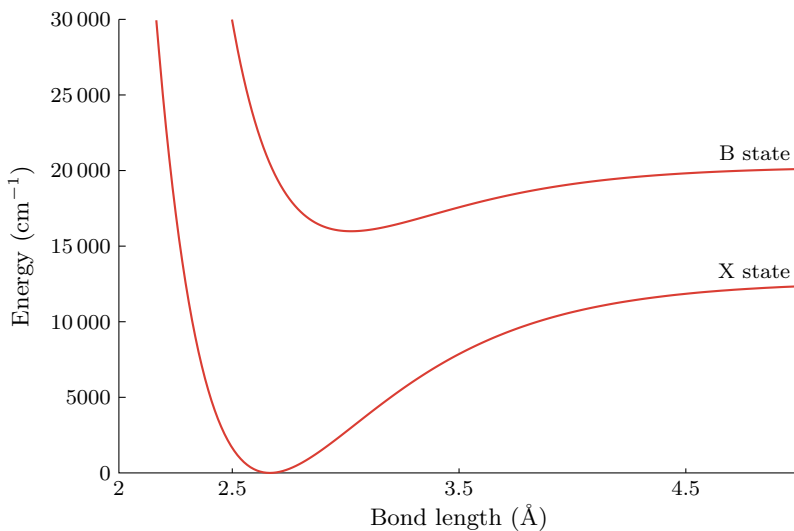


Figure 3: Morse potential curves.

From the above plot, it can be seen that the excited state has a slightly longer average bond length (as is to be expected for a molecule that is vibrating more extremely). Additionally, the ground state energies are generally more concentrated in one area, whereas the excited state ones are more spread out.

Lastly, all of the gas-phase analysis above is compared to the solution phase data. Both the initial data from Figure 1 (or rather a separate data set in terms of the molar extinction coefficient, which is closely related to absorption, obtained from Saiz-Lopez et al. [5]) and the solution-phase data are plotted in Figure 4 on the same set of axes. Expressing the data in terms of molar extinction coefficient is driven by the nature of the data from Saiz-Lopez et al. [5]; data from the solution-phase experiment performed by the authors is readily converted from absorption to molar extinction coefficient using Beer's law (per the introduction). Wavelength has been adjusted for as previously mentioned.

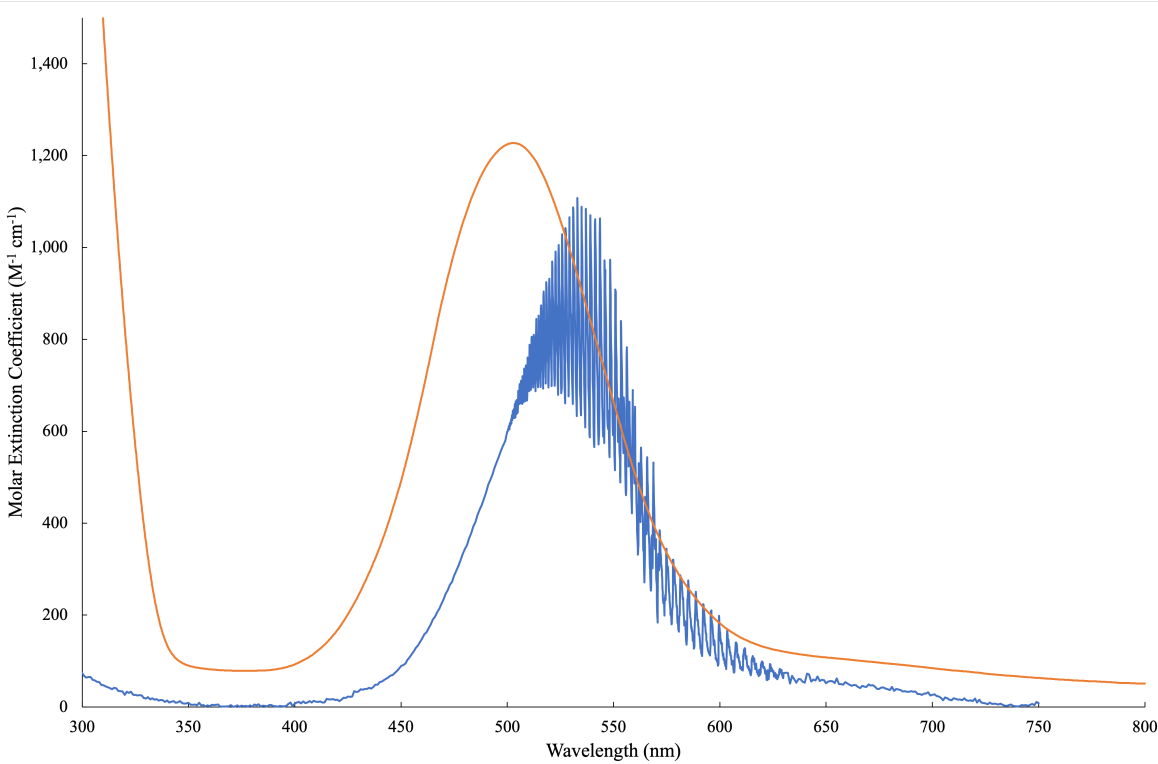


Figure 4: The absorption spectrum (in terms of the directly proportional molar extinction coefficient) of gaseous⁵ (blue) and chloroform-based (orange) I₂ between $\lambda = 300 - 800$ nm.

The maximum of the gas-phase electronic band is $1089 \text{ M}^{-1} \text{ cm}^{-1}$ and occurs at $\lambda = 534.9 \text{ nm}$. The maximum of the solution-phase electronic band is $1227 \text{ M}^{-1} \text{ cm}^{-1}$ at $\lambda = 502.7 \text{ nm}$.

Half the gas-phase electronic maximum is $544.5 \text{ M}^{-1} \text{ cm}^{-1}$. The line $\varepsilon = 544.5 \text{ M}^{-1} \text{ cm}^{-1}$ intersects the left side of the peak at $\lambda = 496 \text{ nm}$ and the right side between $\lambda = 548.1 - 565.8 \text{ nm}$. Taking the average yields

$$\frac{548.1 + 565.8}{2} = 557.0$$

Thus, the full width of the absorption band at half the maximum height (FWHM) is

$$\text{FWHM} = 557.0 - 496 = 61 \text{ nm}$$

Half of the solution-phase electronic maximum is $613.5 \text{ M}^{-1} \text{ cm}^{-1}$. The line $\varepsilon = 613.5 \text{ M}^{-1} \text{ nm}^{-1}$ intersects the left side of the peak at $\lambda_1 = 456.7 \text{ nm}^{-1}$ and the right side at $\lambda_2 = 553.19 \text{ nm}^{-1}$. Therefore, the FWHM is

$$\text{FWHM} = 96.5 \text{ nm}$$

The molar extinction coefficient can be read off the graph above as the electronic maximum, yielding $1227 \text{ M}^{-1} \text{ cm}^{-1}$.

Discussion

Assuming that each vibrational peak corresponds to a Lorentzian lineshape, the “disappearance” of vibrational peaks in the solution phase likely is actually representative of extreme flattening of the peaks. Molecularly, this corresponds to heightened damping of the oscillator, which would make sense in solution as all I₂ molecules will be restricted in motion by the surrounding solvent molecules. Additionally, the electronic blue shift means that more energy in general is required to excite the molecule in solution. One possible factor that could account for the shift in wavelength is that effective wavelength is shortened in substances

(including chloroform) due to their index of refraction. However, this effect is more an empirical one than an actual one (light is just bouncing around more and thus “looks” slower), so this could probably not explain the corresponding energy shift. A better theory is that the ground and excited states actually get farther apart in solution. One potential cause of this is stabilization of the ground state due to solvent effects. This stabilization would not similarly apply to the excited state since by the Born-Oppenheimer approximation, solvent molecules will not have time to rearrange on the timescale of the transition.

For free molecular dynamics, though, it is far more instructive to look at the gas phase. The light excites an electron from its ground electronic state and a ground (or slightly excited) vibrational state to an excited electronic state and a much higher vibrational state in a vibronic transition.

Theory and measured literature values are generally pretty close, and always on the same order of magnitude (sometimes much better). A precise quantitative treatment was not performed, but it can be assumed that this is pretty close, given the crudeness of the setup.

Throughout the experiment, steps were taken to collect baselines and correct for instrumental error. To calibrate the SPEX 500M monochromator, a mercury lamp that emits strongly at one characteristic frequency was used. This known frequency was compared against that recorded by the monochromator and PMT to determine an offset in the values. With the solution-phase setup, both a dark baseline (for system error) and a chloroform/cuvette baseline (for setup error) were subtracted from our final data to hopefully isolate the UV/Vis absorption due to I_2 alone.

However, some error likely remained. For example, the gas-phase spectrum was only measured to 1 Å resolution. The machine was capable of going further, and doing so could have yielded more exact peak assignments. Given that even 1 Å shifts in a few peaks can have a remarkable effect on the ultimate analysis, it is certainly possible that being exact to decimal angstroms could have been helpful. Additionally, the monochromator itself is very old and likely has become less exact with age in ways that even mercury calibration cannot fully account for. The not-super-rigorous exclusion of external light sources could also have lead to error in peak height analysis, perhaps affecting calculations of the electronic band maxima. Possible error could have also come from sublimed iodine on the surface of the tube windows². Human error in the chloroform setup included the fact that the instrument was manually put together and the shield, for instance, could have been in slightly different places each time. Additionally, the dilution was carried out by hand, so there could have been error in the calculation of the concentration of the solution. Moreover, chloroform is very volatile, so subtle concentration changes likely occurred throughout the experiment due to evaporation. On the data-analysis side of things, the Morse potential in and of itself is a crude model. Using the Lennard-Jones potential, for instance, would have been more accurate. Additionally, the anharmonicity was only approximated to first order, not to higher order as it certainly could have been. Thus, the PES's in Figure 3 and data in Table 2 may not even be entirely representative of the data collected.

However, given the remarkable closeness to literature values, the data was likely pretty good with a few of the aforementioned sources of error disproportionately affecting the overall data quality.

Conclusion

The most important results are that solvent effects blue shift the overall transitions between solution-phase and gas-phase data, and that there is an experimental basis for anharmonicity. From Figure 2, a linear fit is not a bad approximation of anharmonicity, so the Morse potential is at least somewhat justified. Further evidence for this justification comes from Verma [4].

The goal of this experiment was to determine several spectroscopic constants of I_2 and use them to calculate the potential energy surface, approximated as a Morse potential, of the ground and second excited states. This was achieved. Additionally, the researchers sought to compare solution-phase and gas-phase data to obtain insight into how phase changes alter molecular dynamics. This was also achieved.

The result is a verification of the quantum-mechanical theory of light absorption. Additionally, this experiment shows that even simple models like the Morse potential can have real predictive power. Separately, it shows that molecular interaction effects in condensed phases (and the lack thereof in expanded phases) have identifiable optical effects.

References

- (1) Huber, K. P.; Herzberg, G. H. In *NIST Chemistry WebBook, NIST Standard Reference Database Number 69*, Linstrom, P. J., Mallard, W. G., Eds., <https://doi.org/10.18434/T4D303>; National Institute of Standards and Technology: Gaithersburg MD, 20899; Chapter Constants of Diatomic Molecules.
- (2) McNaught, I. J. The Electronic Spectrum of Iodine Revisited. *J. Chem. Educ.* **1980**, *57*, 101–105.
- (3) Lant, H. Electronic Spectroscopy: Absorption Spectra of Molecular Iodine in the Gas Phase, Rev. 1-21-23, 2023.
- (4) Verma, R. D. Ultraviolet Resonance Spectrum of the Iodine Molecule. *J. Chem. Phys.* **1960**, *32*, 738–749.
- (5) Saiz-Lopez, A.; Saunders, R. W.; Joseph, D. M.; Ashworth, S. H.; Plane, J. M. C. Absolute absorption cross-section and photolysis rate of I_2 . *Atmos. Chem. Phys.* **2004**, *4*, 1443–1450.
- (6) Seh, Z. W.; Kibsgaard, J.; Dickens, C. F.; Nørskov, J. C. J. K.; Jaramillo, T. F. Combining theory and experiment in electrocatalysis: Insights into materials design. *Science* **2017**, *355*, eaad4998.
- (7) Wuttig, A. Electrochemistry, Video lecture, Chicago, IL: University of Chicago, 2023.
- (8) Laursen, A. B.; Varela, A. S.; Dionigi, F.; Fanchiu, H.; Miller, C.; Trinhammer, O. L.; Rossmeisl, J.; Dahl, S. Electrochemical Hydrogen Evolution: Sabatier’s Principle and the Volcano Plot. *J. Chem. Educ.* **2012**, *89*, 1595–1599.
- (9) Wuttig, A.; Lant, H. Electrokinetics: Mechanism of Hydrogen Evolution on Catalytic Transition and Late Metal Electrodes, 2023.
- (10) Pourbaix, M., *Atlas of Electrochemical Equilibria in Aqueous Solutions*; National Association of Corrosion Engineers: 1440 South Creek Drive, Houston, Texas 77084, 1974.
- (11) Connor, P.; Schuch, J.; Kaiser, B.; Jaegermann, W. The Determination of Electrochemical Active Surface Area and Specific Capacity Revisited for the System MnO_x as an Oxygen Evolution Catalyst. *Z. Phys. Chem.* **2020**, *234*, 979–994.

Steven Labalme
2 February 2023

16 February 2023

4 NMR ANALYSIS OF HEXYLAMINE

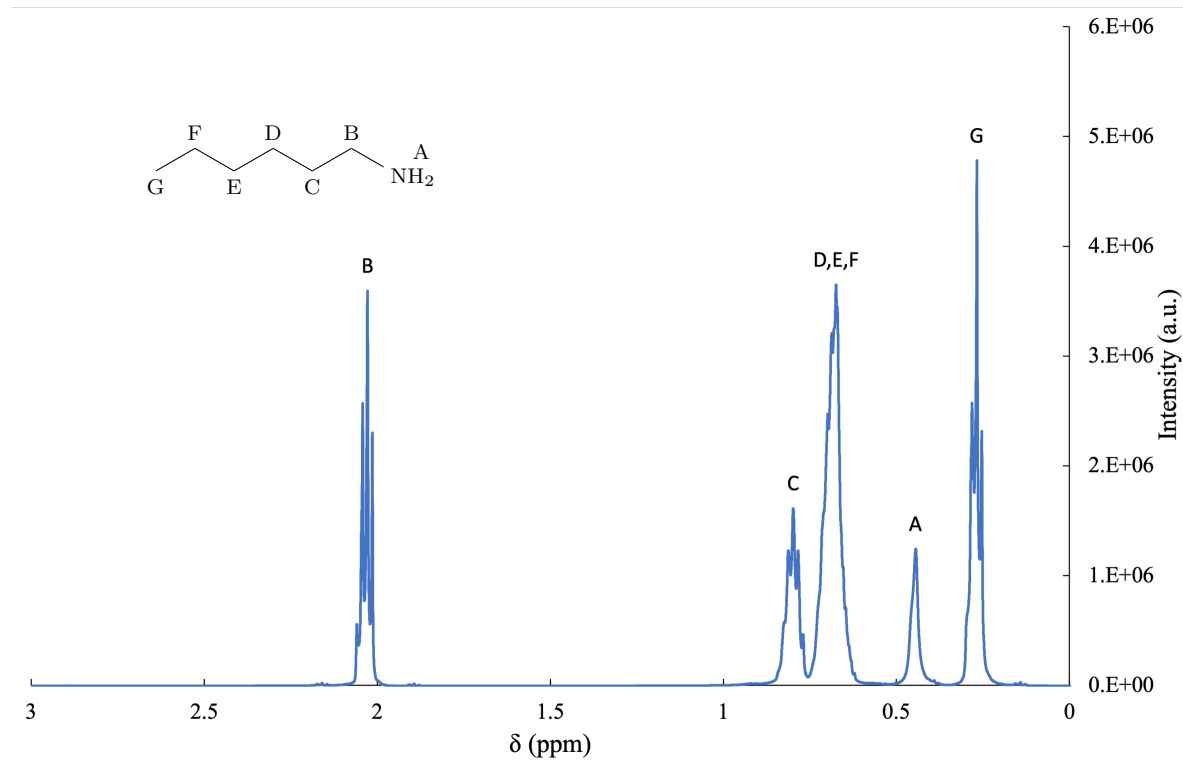


Figure 1: ^1H NMR spectrum of hexylamine. The protons on nitrogen exchange rapidly in solution, so since chemical exchanges cause spin decoupling, the A peak is a singlet.

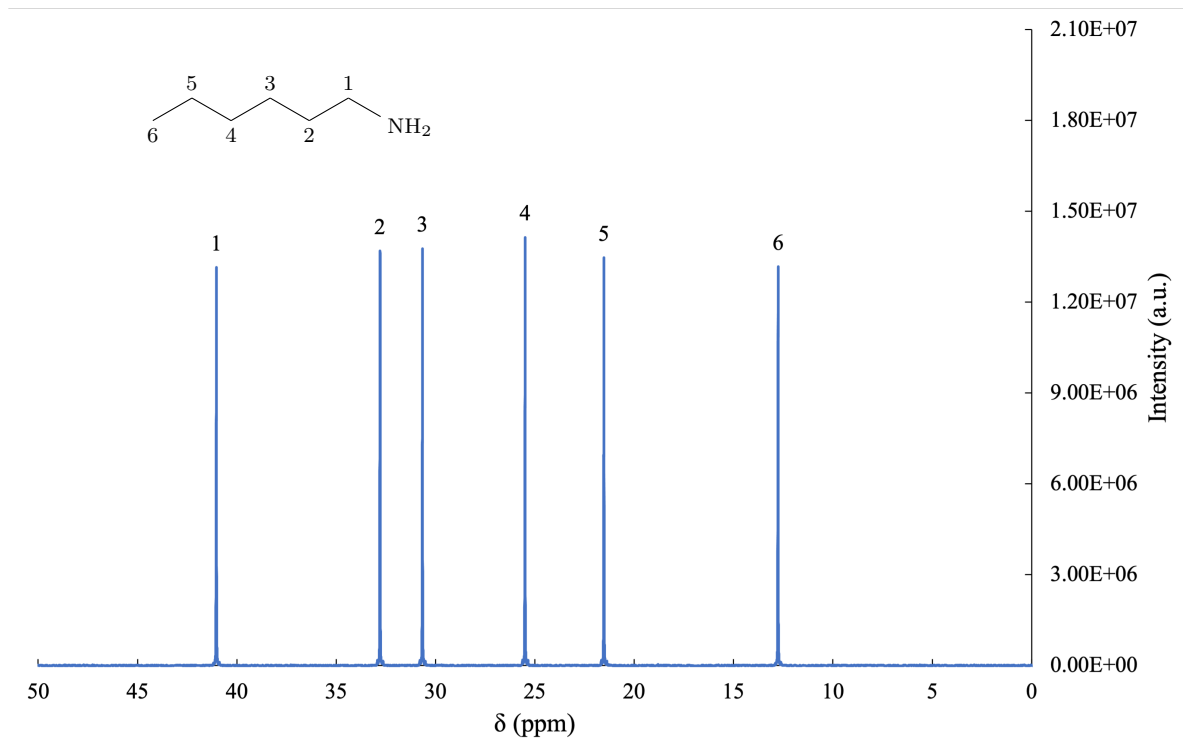


Figure 2: ^{13}C NMR spectrum of hexylamine. Notice that carbon 1 is the most downshifted because it's closest to the electronegative nitrogen atom.

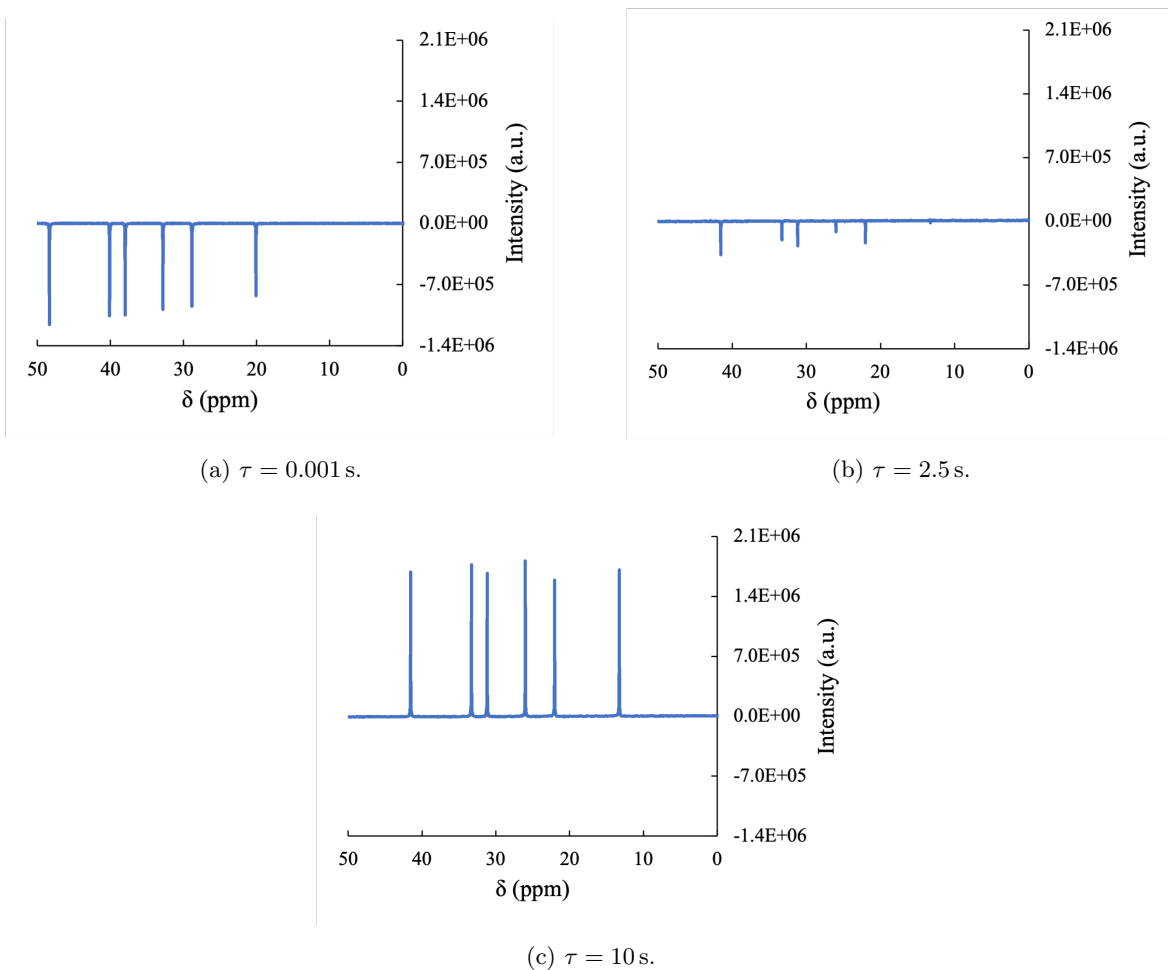


Figure 3: A selection of inversion recovery ^{13}C NMR spectra for different delay times τ .

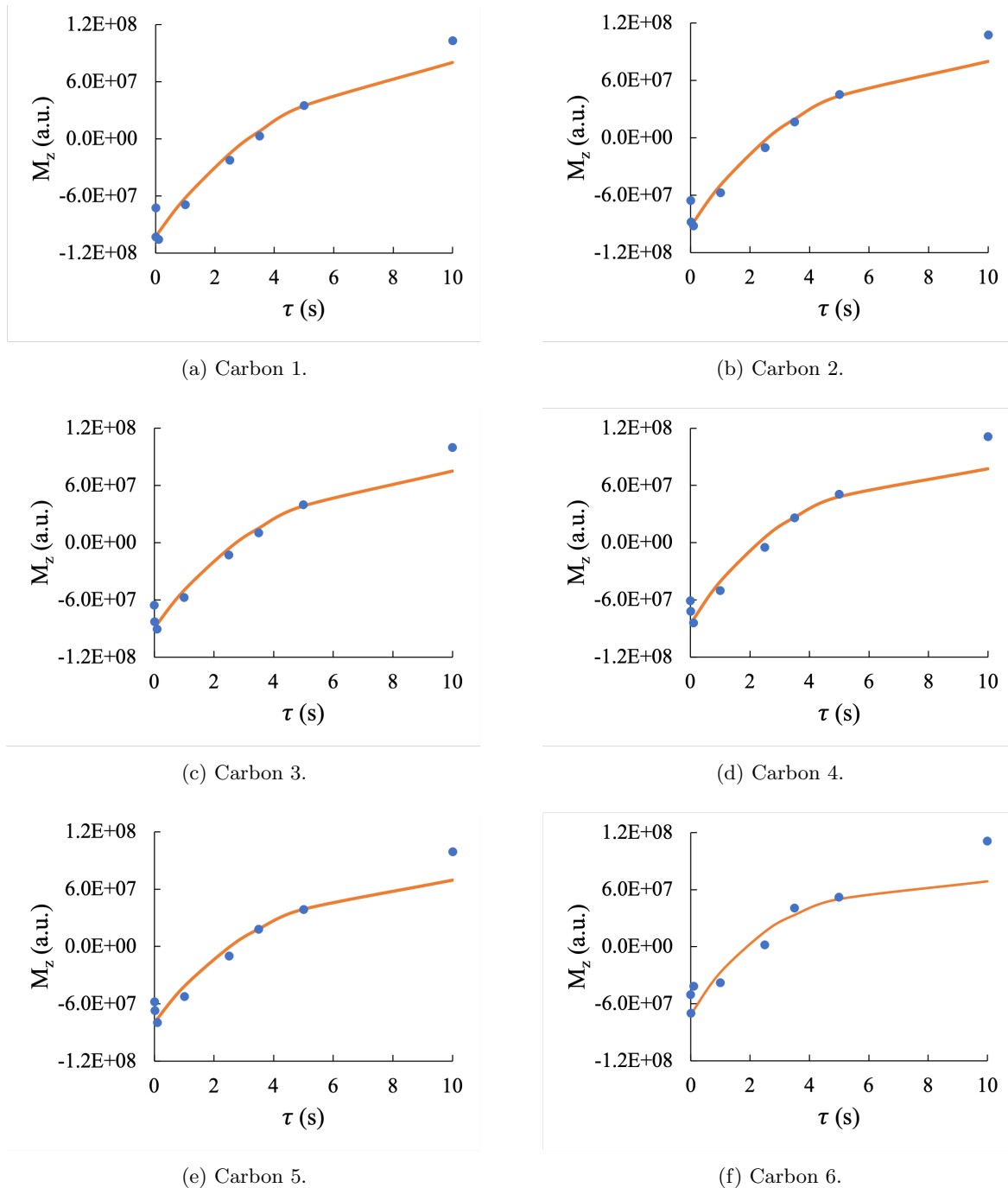


Figure 4: Determining the spin-lattice relaxation time T_1 and the magnetization M_0 at equilibrium via nonlinear regression.

Carbon 1	Carbon 2	Carbon 3	Carbon 4	Carbon 5	Carbon 6
15 197 494.17	15 490 978.25	14 146 608.68	17 608 862.89	15 739 108.37	21 625 158.79

Table 1: Standard errors for the above nonlinear regressions.

	Carbon 1	Carbon 2	Carbon 3	Carbon 4	Carbon 5	Carbon 6
T_1 (s)	4.52	3.75	3.99	3.29	3.67	2.66
τ_C (ps/rad)	5.15	6.21	5.83	7.07	6.34	5.83

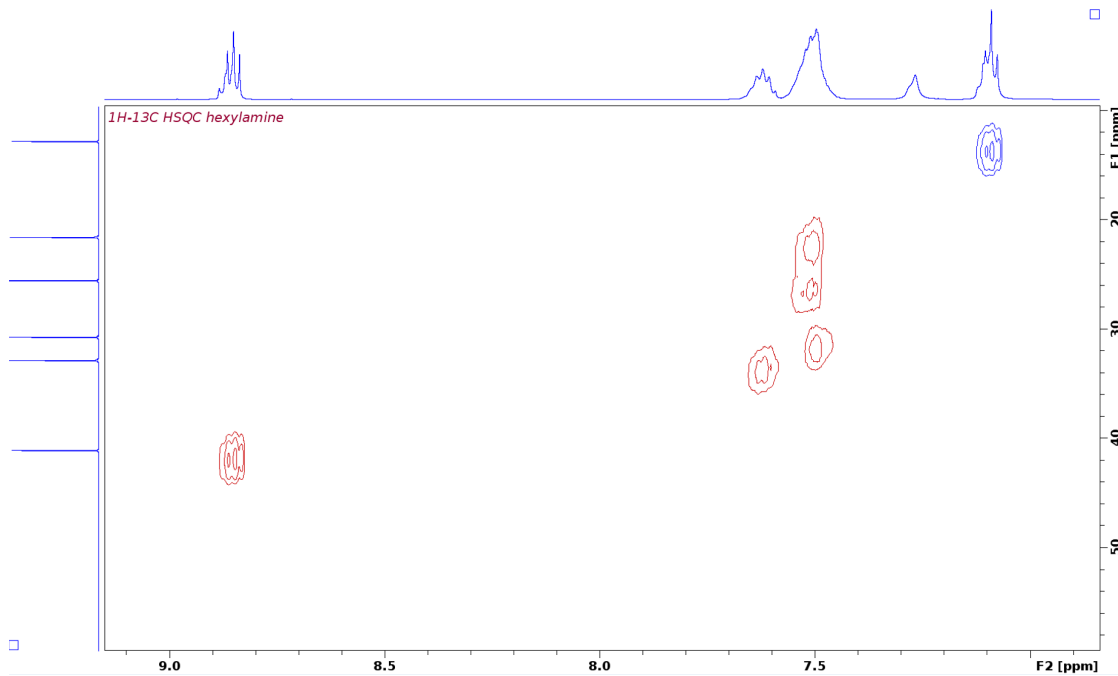
Table 2: The spin-lattice relaxation time and correlation time for each carbon in hexylamine.

Note that to calculate τ_C from T_1 , the formula

$$\frac{1}{T_1} = n \left(\frac{\mu_0}{4\pi} \right)^2 \frac{\hbar^2 \gamma_C^2 \gamma_H^2}{r_{CH}^6} \tau_C$$

was used, where the values of γ_C and γ_H were obtained from [bib:C13H1gyroempty citation](#) and the value of r_{CH} was obtained from [bib:CRCHandbookempty citation](#).

T_1 is the time constant governing how quickly magnetic spins return to equilibrium after a disturbance. The data in Table 2 shows that T_1 trends downward for carbon atoms progressively farther from the amine moiety. This implies that carbons farther from the NH_2 group return to equilibrium more quickly. This would support a theory that the hydrogen-bonding interactions present at the NH_2 group restrict freedom in this molecule, and that portions of it farther from the center of restriction can move more freely and equilibrate more quickly. Since τ_C is related to freedom of motion directly (it is literally a measure of the time required to change angle), the above commentary also applies to it.

Figure 5: Two-dimensional ^1H - ^{13}C HSQC spectrum of hexylamine.

The peaks at the top of the HSQC spectrum in Figure 5 are analogous to those in the ^1H spectrum of hexylamine. Similarly, those on the left side of the above image are analogous to those in the ^{13}C spectrum of hexylamine. HSQC transfers magnetism between bound protons and ^{13}C atoms atoms, so moieties that resonate in both forms of spectroscopy show up as two-dimensional peaks; in other words, each 2D peak corresponds to the proton above it and the carbon to the left of it. Thus, the six distinct peaks in the 2D spectrum correspond to the six carbons and their associated protons. The one hydrogen peak with no corresponding carbon peak represents the protons on the NH_2 moiety, providing additional evidence for the identification of that peak beyond the fact that it's a singlet per rapid proton transfer-induced spin decoupling.

References

- (1) Huber, K. P.; Herzberg, G. H. In *NIST Chemistry WebBook, NIST Standard Reference Database Number 69*, Linstrom, P. J., Mallard, W. G., Eds., <https://doi.org/10.18434/T4D303>; National Institute of Standards and Technology: Gaithersburg MD, 20899; Chapter Constants of Diatomic Molecules.
- (2) McNaught, I. J. The Electronic Spectrum of Iodine Revisited. *J. Chem. Educ.* **1980**, *57*, 101–105.
- (3) Lant, H. Electronic Spectroscopy: Absorption Spectra of Molecular Iodine in the Gas Phase, Rev. 1-21-23, 2023.
- (4) Verma, R. D. Ultraviolet Resonance Spectrum of the Iodine Molecule. *J. Chem. Phys.* **1960**, *32*, 738–749.
- (5) Saiz-Lopez, A.; Saunders, R. W.; Joseph, D. M.; Ashworth, S. H.; Plane, J. M. C. Absolute absorption cross-section and photolysis rate of I_2 . *Atmos. Chem. Phys.* **2004**, *4*, 1443–1450.
- (6) Seh, Z. W.; Kibsgaard, J.; Dickens, C. F.; Nørskov, J. C. J. K.; Jaramillo, T. F. Combining theory and experiment in electrocatalysis: Insights into materials design. *Science* **2017**, *355*, eaad4998.
- (7) Wuttig, A. Electrochemistry, Video lecture, Chicago, IL: University of Chicago, 2023.
- (8) Laursen, A. B.; Varela, A. S.; Dionigi, F.; Fanchiu, H.; Miller, C.; Trinhammer, O. L.; Rossmeisl, J.; Dahl, S. Electrochemical Hydrogen Evolution: Sabatier’s Principle and the Volcano Plot. *J. Chem. Educ.* **2012**, *89*, 1595–1599.
- (9) Wuttig, A.; Lant, H. Electrokinetics: Mechanism of Hydrogen Evolution on Catalytic Transition and Late Metal Electrodes, 2023.
- (10) Pourbaix, M., *Atlas of Electrochemical Equilibria in Aqueous Solutions*; National Association of Corrosion Engineers: 1440 South Creek Drive, Houston, Texas 77084, 1974.
- (11) Connor, P.; Schuch, J.; Kaiser, B.; Jaegermann, W. The Determination of Electrochemical Active Surface Area and Specific Capacity Revisited for the System MnO_x as an Oxygen Evolution Catalyst. *Z. Phys. Chem.* **2020**, *234*, 979–994.

Steven Labalme
9 February 2023

23 February 2023

5 GCMS ANALYSIS OF BENZENE IN GASOLINE

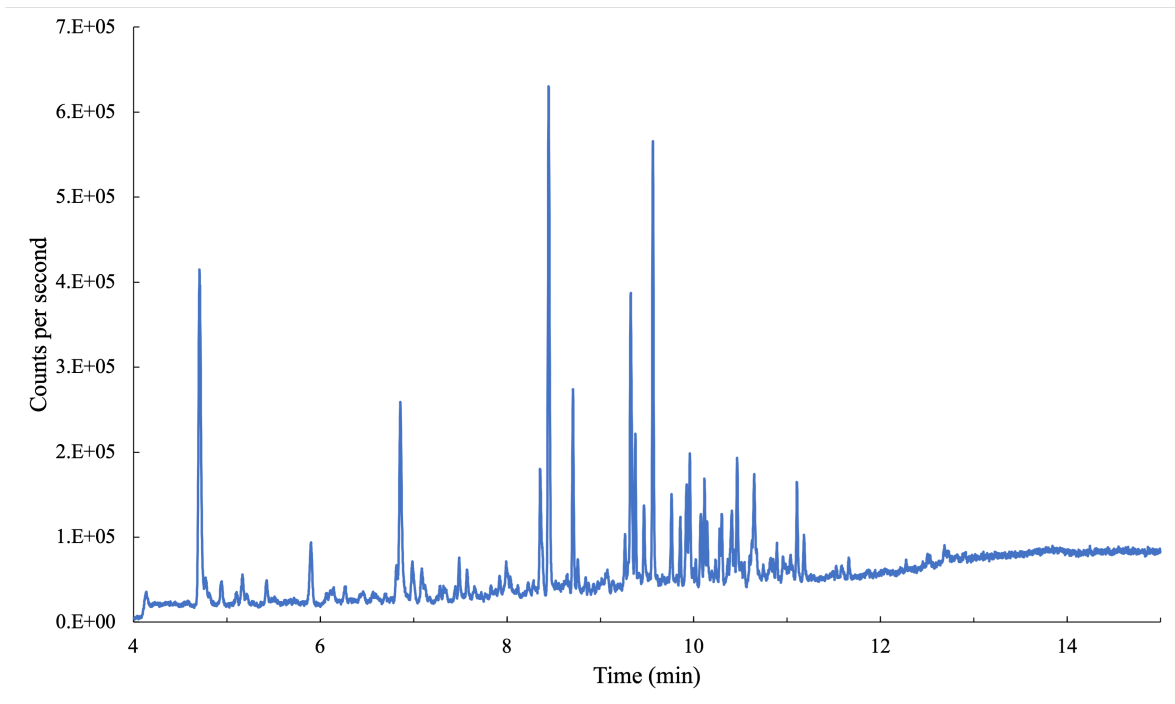


Figure 1: Total ion chromatogram of diluted 87-gasoline in pentane.

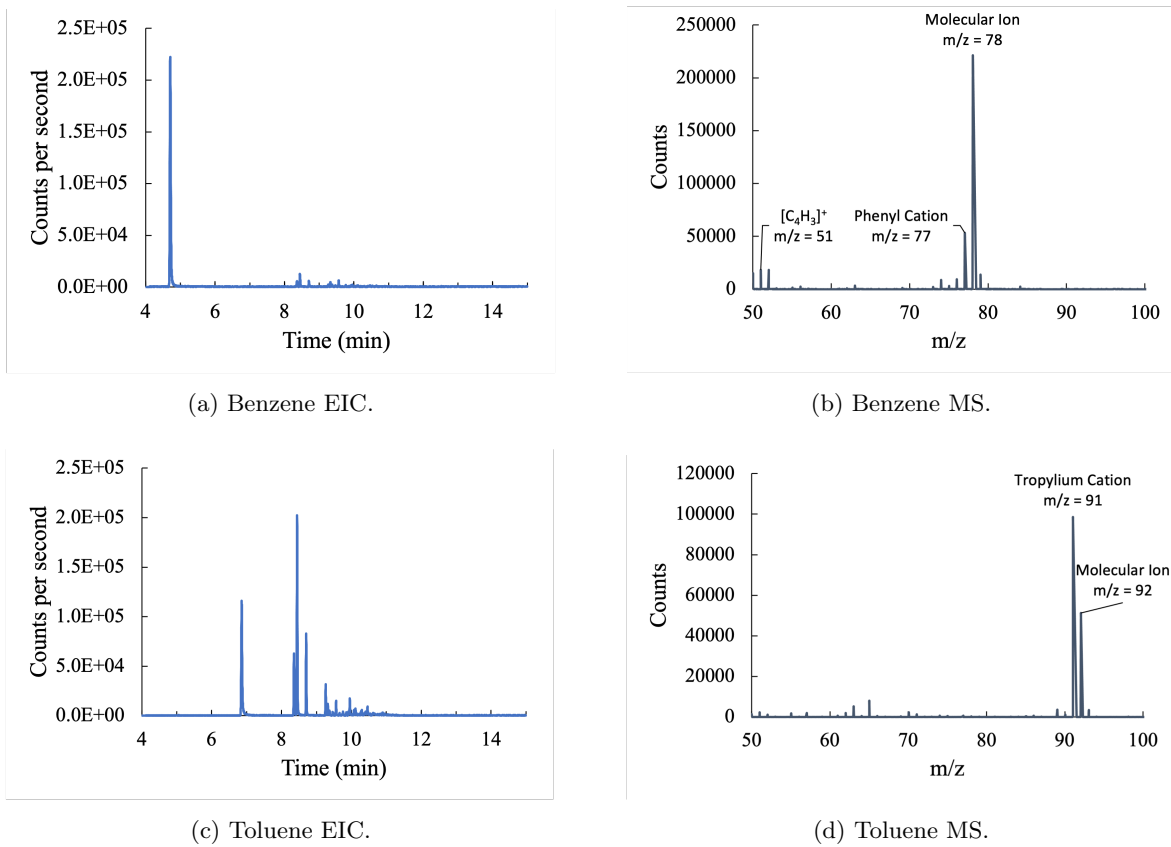


Figure 2: Extracted ion chromatograms and extracted mass spectra for benzene and toluene.

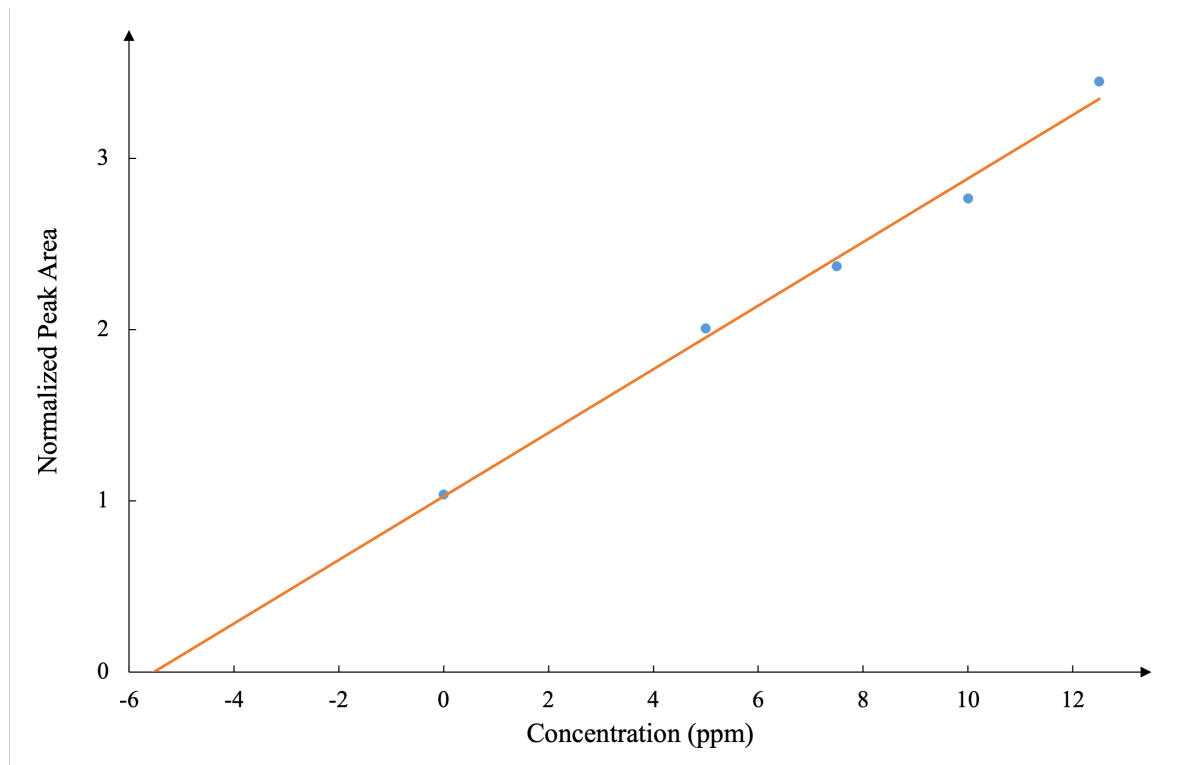


Figure 3: Standard addition of benzene.

Concentration (v/v)	Error (v/v)
3.95×10^{-4}	$\pm 1.66 \times 10^{-4}$

Table 1: Concentration of benzene in gasoline.

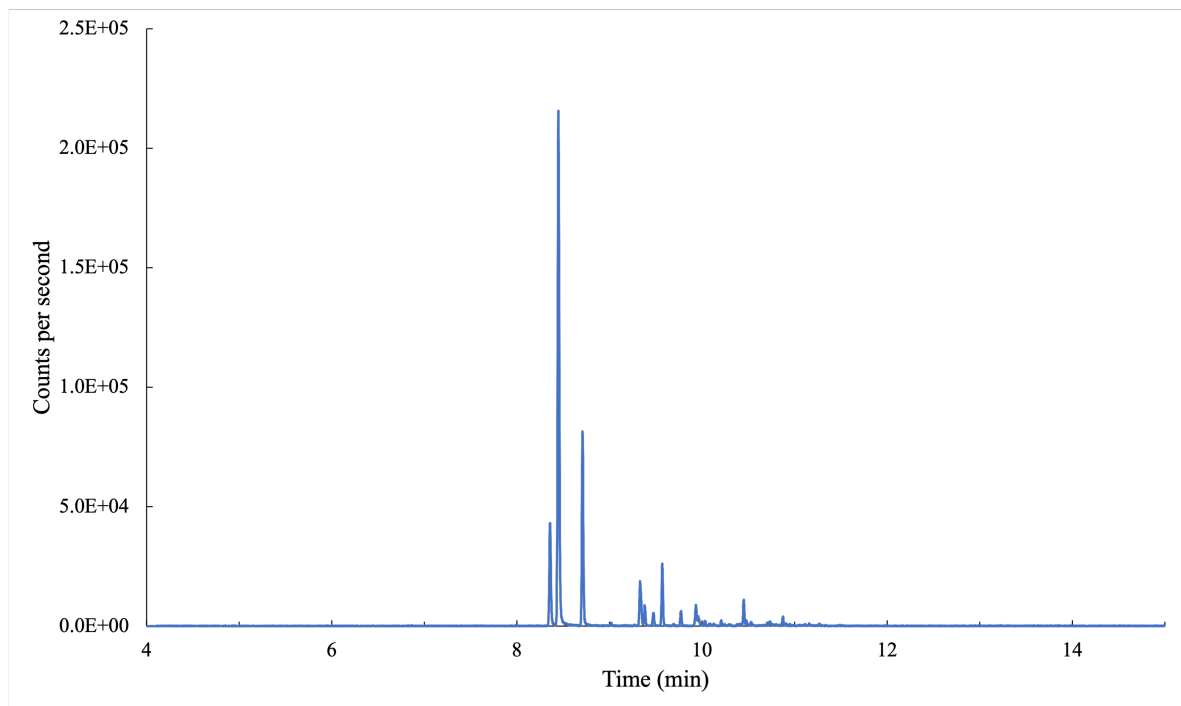


Figure 4: Extracted ion chromatogram of ethylbenzene.

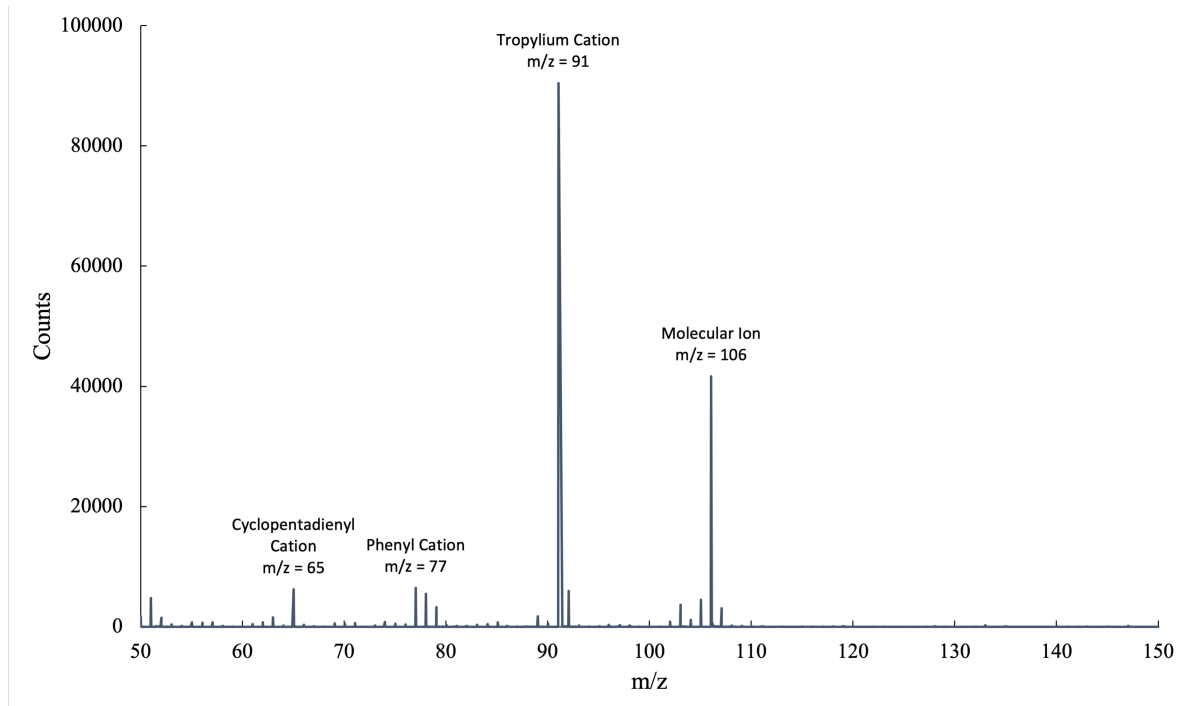


Figure 5: Extracted mass spectra of ethylbenzene.

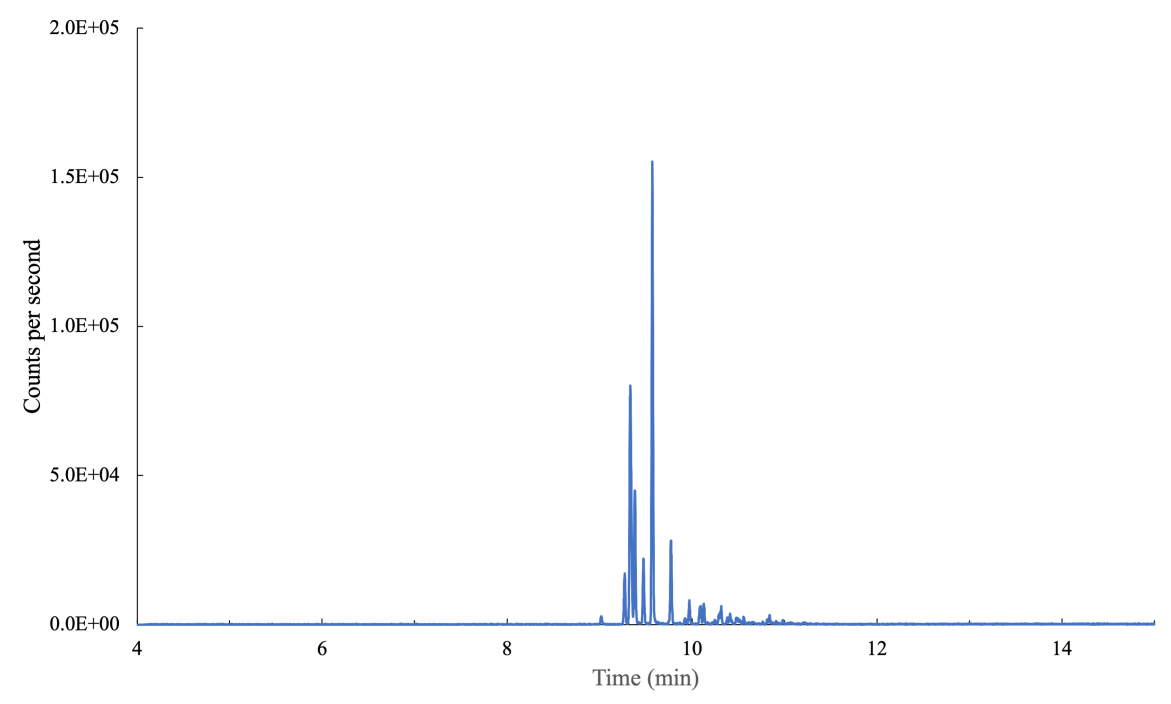


Figure 6: Extracted ion chromatogram of mesitylene.

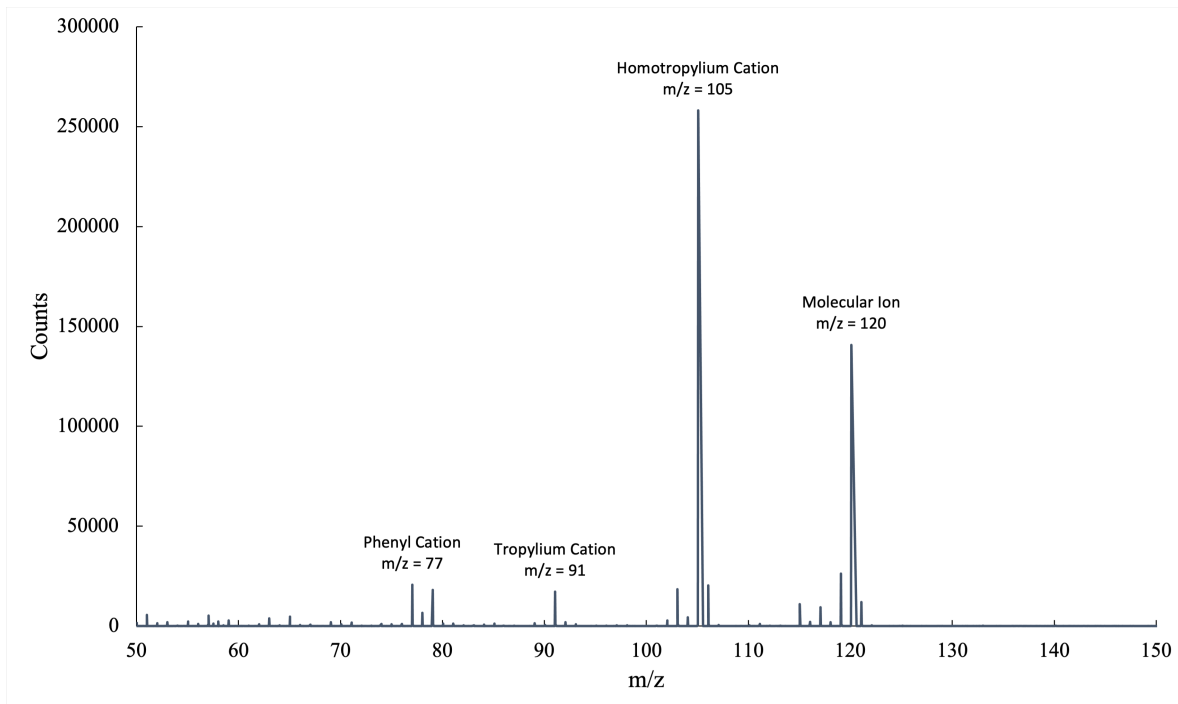


Figure 7: Extracted mass spectra of mesitylene.

	Ethylbenzene	Mesitylene
Concentration (ppm)	1.71	2.48

Table 2: Concentrations of additional aromatic molecules.

These substances may not follow the same peak area-to-concentration fit as benzene (Figure 3). Indeed, to more accurately determine the concentrations of these substances in gasoline, it would be appropriate to do a standard addition analysis for both of them, individually, instead of relying on more distantly related correspondences.

Steven Labalme

TA: Ben Masters

Lab partners: Joe Geniesse, Irene Madejski, and Sophia Madejski

16-23 February 2023

2 March 2023

6 ANALYSIS OF THE ELECTROCATALYTIC ACTIVITY OF PLATINUM, TIN, AND TITANIUM TOWARD THE HYDROGEN EVOLUTION REACTION

Abstract

The goal of this experiment is to evaluate three candidates for the electrocatalysis of the hydrogen evolution reaction (a reaction in which there is broad chemical and societal interest), and to probe the mechanism over each of metal to determine which of two well-defined types is active. It was determined that the order of catalytic activity is platinum, then titanium, then tin. Additionally, it was determined that platinum follows the Volmer-Tafel mechanism with second-order reaction kinetics in the concentration of acid, and tin follows the Volmer-Heyrovsky mechanism with first-order kinetics in said concentration. Altogether, the data suggests that the metal-hydride bond strength is a key indicator of the rate of the hydrogen evolution reaction, providing a key tool necessary to design future reactions.

Introduction

The constantly increasing societal demand for energy coupled with the perils of climate change demand investment in sustainable, fossil-fuel free sources of energy. One direction that has been attracting increasing interest is electrochemistry; promising experiments suggest that important problems in chemical synthesis, renewable energy, energy storage, and more may be able to be solved using such an approach.⁶ For example, means of harnessing the carbon dioxide reduction reaction to store wind and solar energy have been devised and implemented at small scales.⁷

Electrochemistry is particularly interesting because it is comparably simple to probe the mechanisms of electrochemical reactions, a rarity in chemistry.⁷ For example, the reaction rate is always directly measurable via its direct proportionality with the flowing current. Indeed, since the mechanisms are well-understood, rational design of experiments is commonplace. For example, a molecular-level understanding of the hydrogen evolution reaction (HER) allows scientists to predict that changing the concentration of an acid *molecule* (the hydronium producing species) will affect the reaction rate, but changing the level of hydronium itself will not. The HER is as follows.



In fact, the HER is particularly notable for several more reasons. Most importantly, it

is key to the production of hydrogen, a promising alternative fuel and valuable commodity chemical. Additionally, it has a very simple mechanism, so strategies to control and manipulate it can be evaluated in theory with relative ease. Thus, optimizing the HER is both desirable (because of its importance in chemistry) and theoretically feasible (because of its simple mechanism). Two important strategies to this effect are (1) selecting the best possible catalyst material and (2) determining which of the two possible mechanisms (Volmer-Tafel [V-T] and Volmer-Heyrovsky [V-H])⁸ is active for a given catalyst material. Both strategies will be worked through herein. The first will be discussed in greater detail presently.

In this study, the researchers will evaluate the electrocatalytic properties of three transition metals: platinum (Pt), tin (Sn), and titanium (Ti). Transition metals are natural candidates for electrocatalysts because of their incompletely filled *d* orbitals, which enable them to donate and accept electrons with a minimal energy penalty. Using cyclic voltammetry (CV), the overpotential η needed to initiate the catalytic reaction will be determined. Measuring against an Hg/HgSO₄ electrode with a potential of 0.650 V vs SHE (SHE is the standard hydrogen electrode, which is the potential of the HER in 1 M acid conditions and under 1 atm of H₂), all data will need to be converted to SHE via

$$E_{\text{SHE}} = E_{\text{Hg/HgSO}_4} + 0.650 \quad (2)$$

All quantities above are in V, a measure of electric potential. The overpotential, specifically, is then given by

$$\eta = E_{\text{H}^+/\text{H}_2} - E_{\text{app}} \quad (3)$$

where $E_{\text{H}^+/\text{H}_2} = 0$ is the potential of the HER vs SHE and E_{app} is the potential applied to induce catalysis. All quantities are, again, in V.

The magnitude of the overpotential reflects the magnitude of the kinetic barriers preventing a particular metal from engaging in catalysis. Thus, it is inversely proportional to the activity of the catalysts, with higher overpotentials signifying greater element-specific kinetic barriers and thus lower activity.

Additionally, the overpotential aids in the design of the subsequent chronoamperometry (CA) experiments. CA data can be collected in the vicinity of the onset potential to enable the construction of a *Tafel plot*. The slope of the line of best fit in this plot is related to some key quantitative differentiators between the V-T and V-H mechanisms, so making one allows for the determination of the active mechanism.

In particular, a Tafel plot plots applied potential on the *y*-axis and the base 10 logarithm of the negative of *current density* on the *x*-axis. Note that the current density is denoted by

j and defined as follows, where I is current and A is geometric surface area.

$$j = \frac{I}{A} \quad (4)$$

Current density is an *intensive* property of the given substance (metal) and is thus a better, normalized measure of activity than raw intensity I , an *extensive* property. It is measured in mA/cm². By definition, it encapsulates the amount of electrons flowing through a unit of area in a given amount of time.

Returning to Tafel plots, the Tafel slope can be related to the molecular parameters as follows.⁹ Begin with the equation

$$j = j_0 e^{\beta \eta F / RT} \quad (5)$$

where j is the measured current density, j_0 is the initial current density, β is the symmetry factor (a unitless measure of the reorganization energy in solution), η is the overpotential, $F = eN_A$ is Faraday's constant, R is the ideal gas constant, and T is temperature. Rearranging, the following is obtained.

$$\begin{aligned} j_0 e^{\beta \eta F / RT} &= j \\ \frac{\beta \eta F}{RT} \log_{10}(e) &= \log_{10} \frac{j}{j_0} \\ \eta &= \frac{1}{\log_{10}(e)} \frac{RT}{\beta F} [\log_{10}(j) - \log_{10}(j_0)] \\ &= 2.3 \frac{RT}{\beta F} [\log_{10}(j) - \log_{10}(j_0)] \end{aligned} \quad (6)$$

Thus, the expected slope of the Tafel plot in terms of molecular parameters is $2.3RT/\beta F$. It follows via consideration of both mechanisms that

$$\frac{2.3RT}{\beta F} = 30 \text{ mV}/\log(j) \quad (7)$$

if the V-T mechanism is active

$$\frac{2.3RT}{\beta F} = 120 \text{ mV}/\log(j) \quad (8)$$

if the V-H mechanism is active. All data fittings will be performed in Excel with a linear regression.

Essentially, the researchers seek herein to determine both which catalyst (between Pt, Sn, and Ti) is the most active and which mechanism (V-T or V-H) is active for Pt and Sn using cyclic voltammetry and the evaluation of the slope of a relevant Tafel plot.

Experimental

The experimental setup used herein centered around a Gamry potentiostat. This device enables the application of precise voltages and the measurement of precise currents to the electrochemical system of interest. All data was collected and interpreted with the help of the Gamry Framework software.

Throughout the laboratory component of the experiment, nitrile gloves, lab coats, and splash goggles were used for personal safety. Additionally, to lessen the likelihood of electrocution by the potentiostat, the researchers held one hand behind their back when interacting with active electrodes.

In the actual experiment, the first electrode tested was the platinum electrode. Before it was inserted into the main setup (Figure 1), it was polished with alumina and milliQ water to remove any corrosion and then sonicated to remove any excess alumina. The experimental setup was then assembled as pictured in Figure 1. All electrodes were submerged in the 0.1 M H₂SO₄ solution and separated from any mutual contact. Sparging was performed with a N₂ needle to remove any excess gas. The open circuit potential and uncompensated resistance were then measured and recorded.

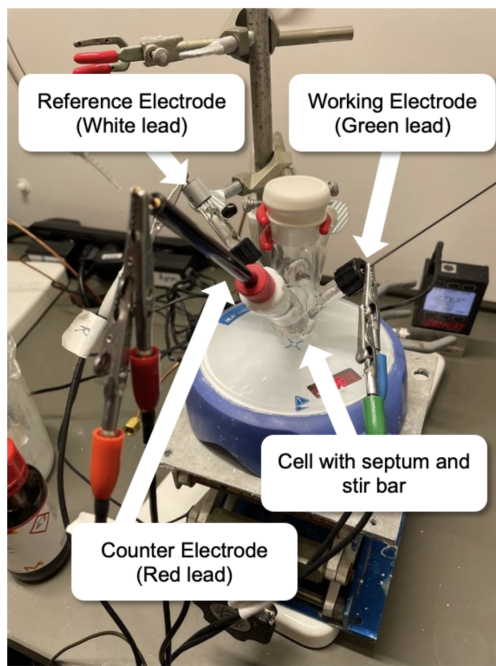


Figure 1. Experimental setup of the electrochemical cell. The three electrodes (working, reference, and counter) can be seen as well as the container in which the reaction took place. Not immediately pictured is the nitrogen needle used for pre-reaction sparging.

Ten cycles of a cyclic voltammogram were then taken from 0 V to -0.8 V and back again, and data was recorded vs a Hg/HgSO₄ reference electrode at a scan rate of 100 mV/s. A catalytic wave was observed, and eleven points surrounding its foot were selected for

chronoamperometry. These points were evenly spaced in 25 mV intervals. Then, using the computer, the potentiostat was instructed to run the different voltages sequentially from least to greatest. Each voltage was run for 100 s and the diameter of the circular platinum surface was noted to be 2 mm for the purpose of subsequent current density calculations. Throughout the initial (platinum) experiment, continuous stirring should have been applied but was not. However, this did not significantly affect the data, per the TA and lab instructor.

The process was repeated for the Sn and Ti electrodes with stirring enabled, as it should have been. The respective areas of these rectangular electrode was measured with a hand ruler to be 6 mm × 8 mm and 7 mm × 9 mm. The respective CVs were collected over 0 V to −1.8 V and 0 V to −1.6 V. Due to extreme corrosion and contamination of the solution with tin oxides during the tin experiment, the electrolyte solution was changed between the tin and titanium runs.

Lastly, the system was cleaned by safely disposing of the acid electrolyte solution, rinsing everything with milliQ water, and returning all components to their initial spaces.

Results and Discussion

As described above, the first step was taking cyclic voltammograms for each electrode and replotting the data on an SHE scale, and plotting the *y*-axis as both current and current density.

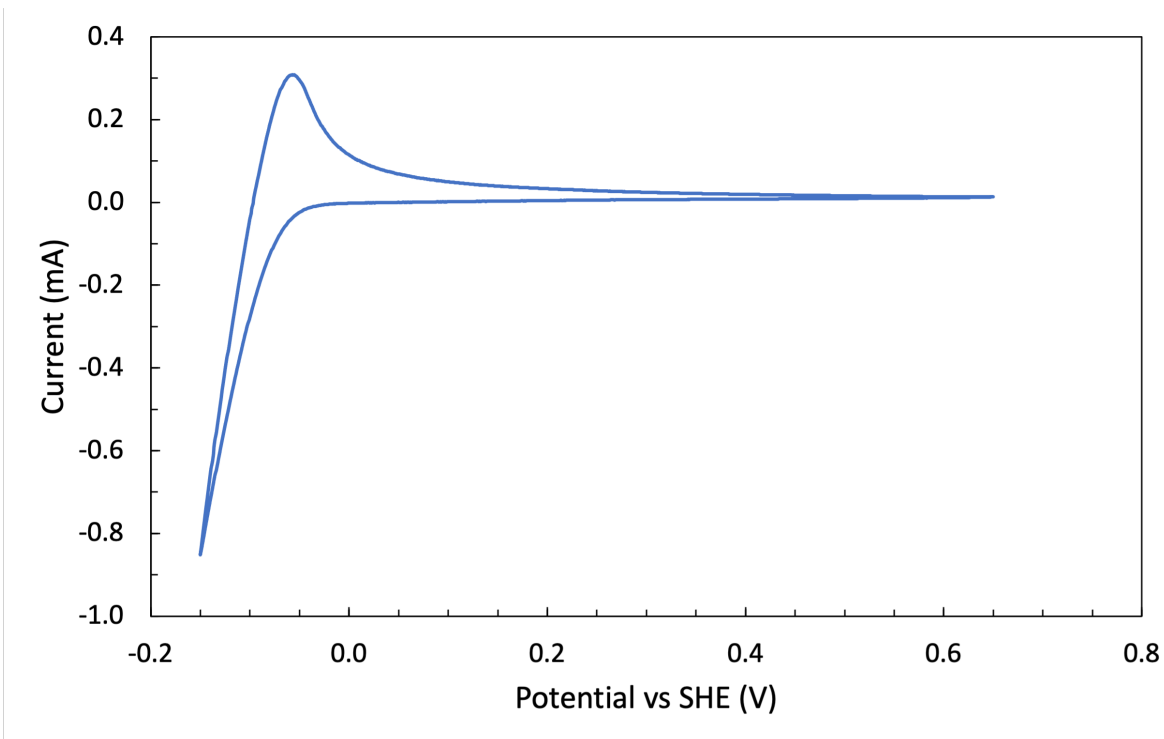


Figure 2. Extensive cyclic voltammogram exhibiting the HER over a Pt electrode in 0.1 M H₂SO₄. The current (in mA) flowing through the working electrode was measured against the applied potential (in V) as the potential ranged from 0.65 V to −0.15 V vs SHE and back again at a scan rate of 100 mV/s. A middle curve (Curve 4) was selected as representative and plotted in Excel. The HER begins at an overpotential of 0.02 V vs SHE on the negative scan, and remaining hydrides are oxidized off of the electrode surface on the positive scan resulting in the peak between −0.1–0 V.

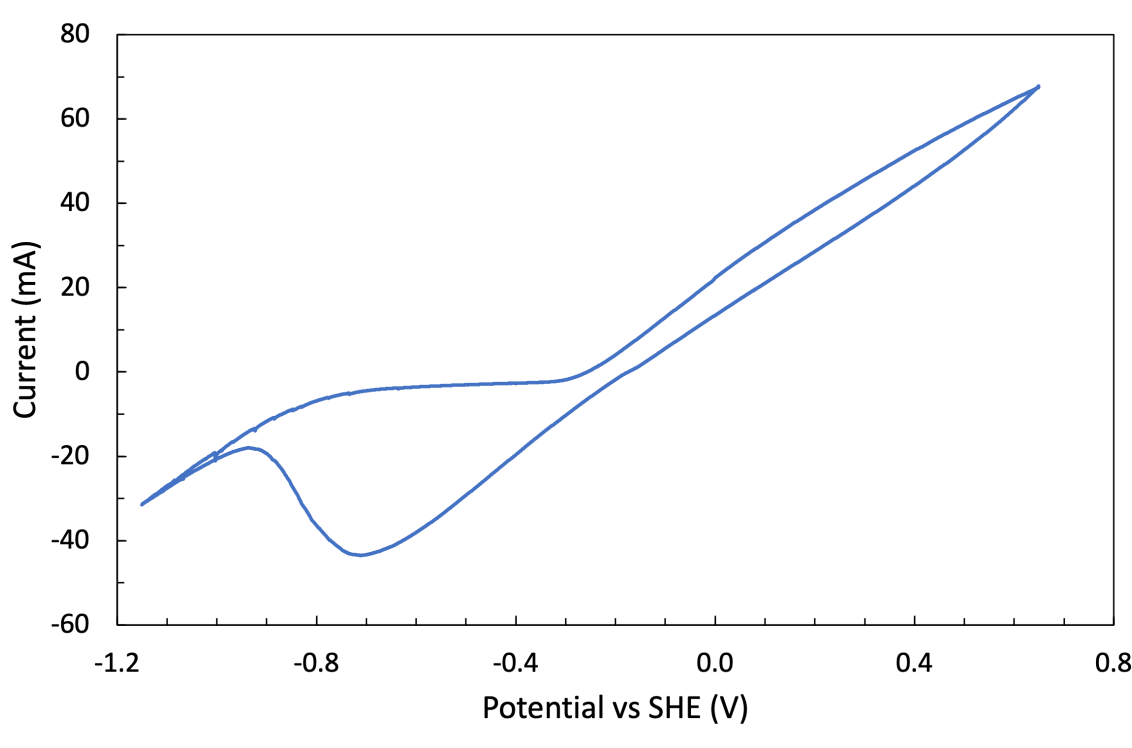


Figure 3. Extensive cyclic voltammogram exhibiting the HER over a Sn electrode in 0.1 M H₂SO₄. The current (in mA) flowing through the working electrode was measured against the applied potential (in V) as the potential ranged from 0.65 V to −1.15 V vs SHE and back again at a scan rate of 100 mV/s. A middle curve (Curve 4) was selected as representative and plotted in Excel. The HER begins at an overpotential of 0.9 V vs SHE on the negative scan. No apparent feature correlates with the oxidation of remaining hydrides off of the electrode surface on the positive scan.

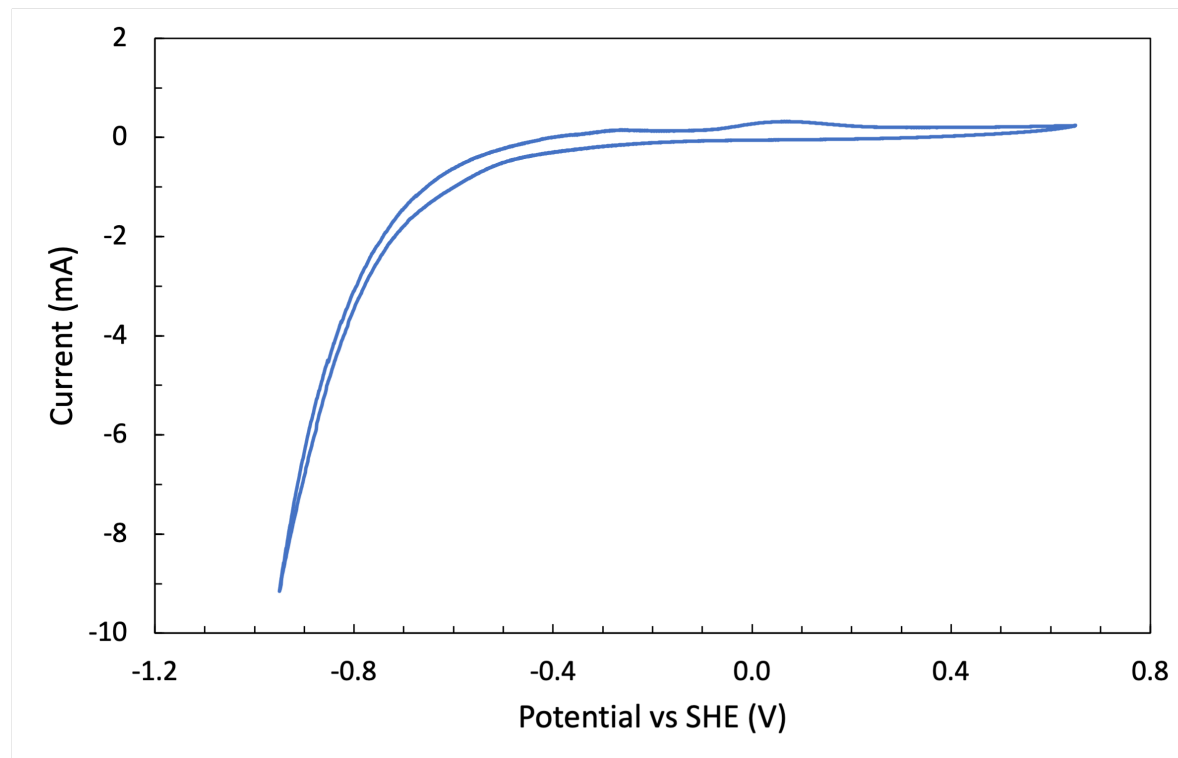


Figure 4. Extensive cyclic voltammogram exhibiting the HER over a Ti electrode in 0.1 M H₂SO₄. The current (in mA) flowing through the working electrode was measured against the applied potential (in V) as the potential ranged from 0.65 V to −0.95 V vs SHE and back again at a scan rate of 100 mV/s. A middle curve (Curve 4) was selected as representative and plotted in Excel. The HER begins at an overpotential of 0.4 V vs SHE on the negative scan, and remaining hydrides are oxidized off of the electrode surface on the positive scan resulting in the peak between 0–0.2 V.

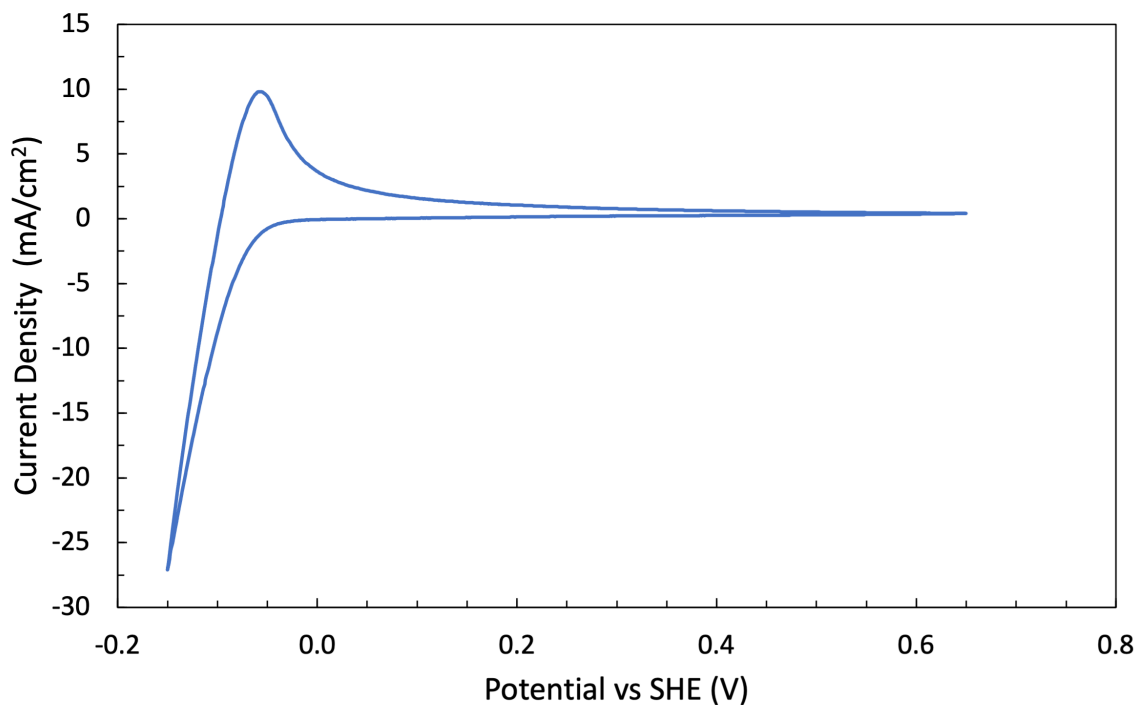


Figure 5. Intensive cyclic voltammogram exhibiting the HER over a Pt electrode in 0.1 M H₂SO₄. The current density (in mA/cm²) flowing through the working electrode was measured against the applied potential (in V) as the potential ranged from 0.65 V to -0.15 V vs SHE and back again at a scan rate of 100 mV/s. The surface area of the catalyst used in the normalization was 0.0314 cm². A middle curve (Curve 4) was selected as representative and plotted in Excel. The HER begins at an overpotential of 0.02 V vs SHE on the negative scan, and remaining hydrides are oxidized off of the electrode surface on the positive scan resulting in the peak between -0.1-0 V.

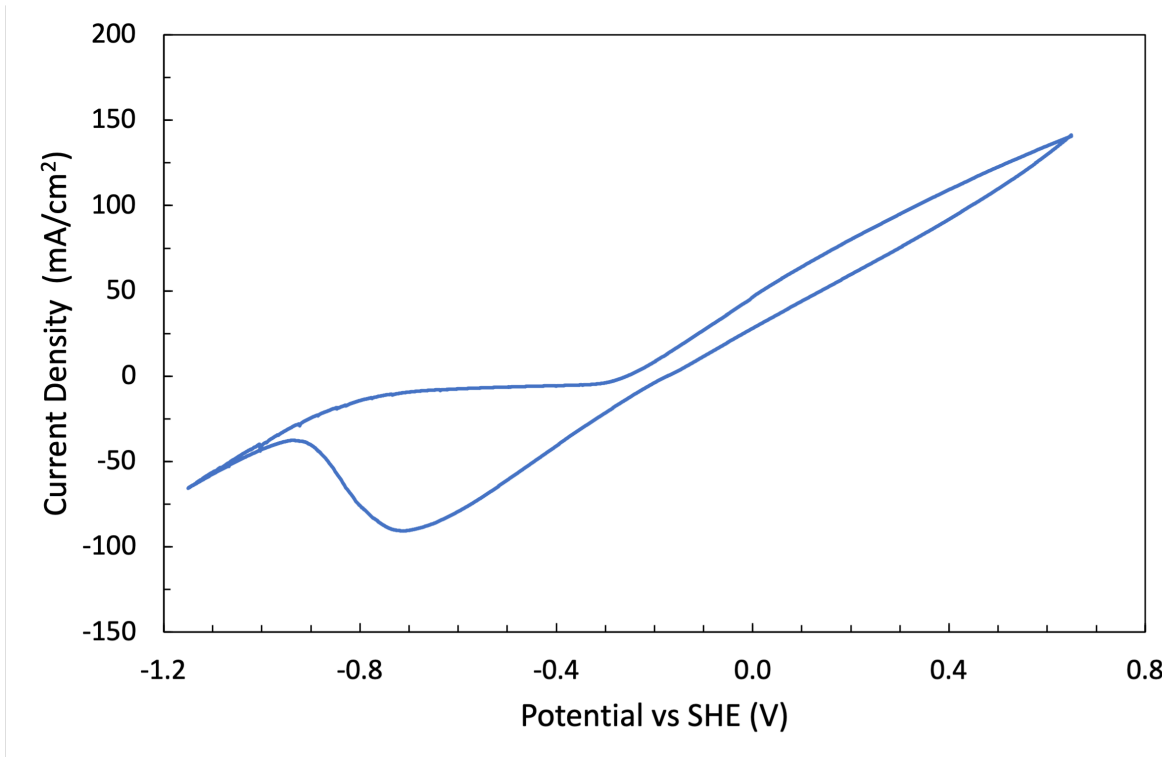


Figure 6. Intensive cyclic voltammogram exhibiting the HER over a Sn electrode in 0.1 M H₂SO₄. The current density (in mA/cm²) flowing through the working electrode was measured against the applied potential (in V) as the potential ranged from 0.65 V to −1.15 V vs SHE and back again at a scan rate of 100 mV/s. The surface area of the catalyst used in the normalization was 0.48 cm². A middle curve (Curve 4) was selected as representative and plotted in Excel. The HER begins at an overpotential of 0.9 V vs SHE on the negative scan. No apparent feature correlates with the oxidation of remaining hydrides off of the electrode surface on the positive scan.

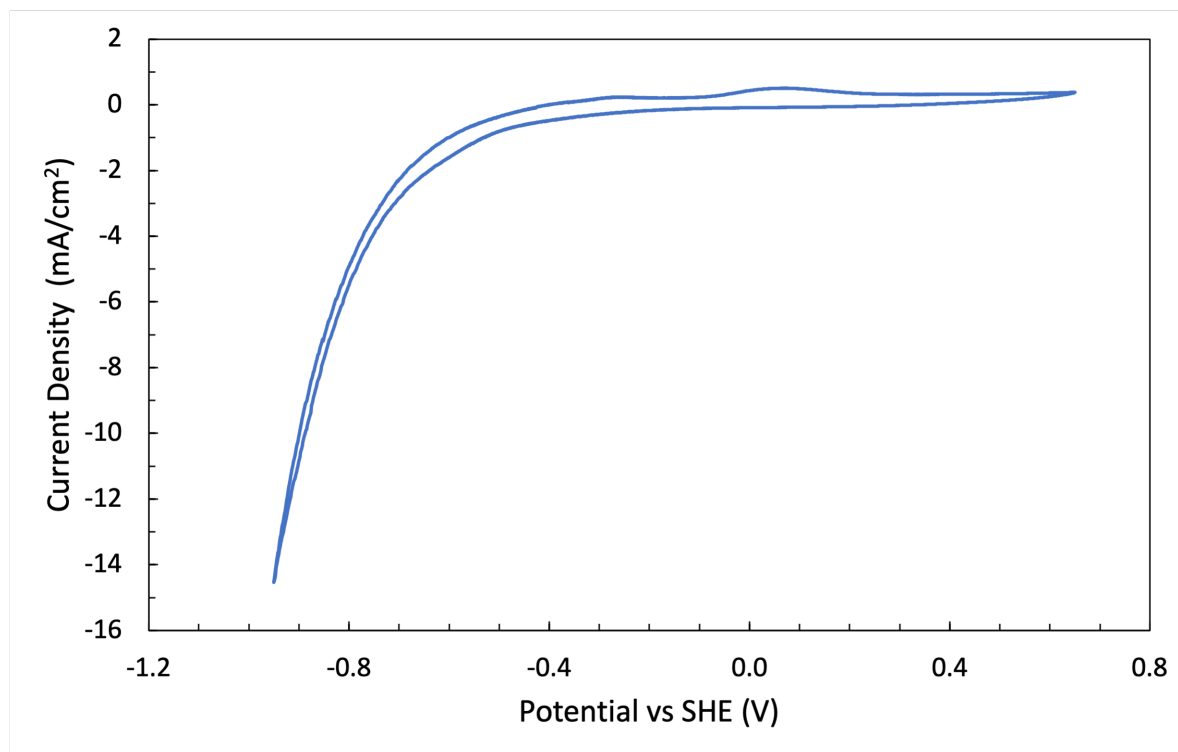


Figure 7. Intensive cyclic voltammogram exhibiting the HER over a Ti electrode in 0.1 M H₂SO₄. The current density (in mA/cm²) flowing through the working electrode was measured against the applied potential (in V) as the potential ranged from 0.65 V to −0.95 V vs SHE and back again at a scan rate of 100 mV/s. The surface area of the catalyst used in the normalization was 0.63 cm². A middle curve (Curve 4) was selected as representative and plotted in Excel. The HER begins at an overpotential of 0.4 V vs SHE on the negative scan, and remaining hydrides are oxidized off of the electrode surface on the positive scan resulting in the peak between 0-0.2 V.

Since H₂SO₄ is a strong diprotic acid, it is safe to assume that it fully dissociates into two equivalents of protons in aqueous solution. Thus,

$$\text{pH} = -\log[\text{H}_3\text{O}^+] = -\log(0.2) \approx 0.7 \quad (9)$$

Based on the Pourbaix diagrams, all three metals at pH = 0.7 cross the HER line (a) at approximately E = 0 V. This agrees well with the foot of the catalytic wave for platinum (see Figures 2, 5), but differs significantly for the feet of the catalytic waves for tin and titanium (see Figures 3-4, 6-7). Additionally, the Pourbaix diagram reveals that at higher potentials, the tin electrode forms tin oxides (largely SnO and SnO₂).¹⁰ These likely account for the significant observed corrosion, as high potentials can oxidize the tin atoms at the surface, making them susceptible to nucleophilic attack by the oxygen atoms of water molecules in solution. Note that the extreme corrosion of the tin electrode and presence of additional electrochemical processes (oxide formation) means that the CV measurement and onset potential calculation for the tin electrode is likely not reliable.

Thus, the result (supported by both the raw current and current density data) that tin is the most active HER catalyst is likely untrue. Consequently, only platinum and titanium will be considered in this analysis. Both the raw current and the current density data (in particular, the position of the onset potentials) indicate that platinum is more active.

Although it didn't matter in this case, note that the plot of current *density* vs. voltage is a more accurate reflection of the intrinsic activity of each electrode material than the plot of raw current vs. voltage. This is because naturally a larger quantity of material will transfer more electrons by virtue of sheer active site size. However, this is an *extensive* property, and normalizing for the surface area allows for the comparison of *intensive* properties of the material. These are actually characteristic and thus of greater interest and validity. See the Introduction for more detail on extensive and intensive properties.

Additionally, while normalization by the geometric surface area is good, alternate methods of normalization may yield even better data. One example is the determination of the *electrochemical active* surface area.¹¹ On an atomic scale, not all sites on the surface of the electrode will be equally conducive to electrochemistry, so directly measuring which ones are can give a more accurate representation of current density.

Returning to the earlier idea of onset potential, recall that the onset potential was determined by analyzing points at the foot of the catalytic waves. This region of high change in current makes it naturally suited to collecting CA data. Thus, chronoamperograms were collected at the onset potential, at five higher potentials, and at five lower potentials. The potentials were all equally spaced 25 mV apart. This allowed for the construction of the Tafel plots below. For the exact method of construction, see the relevant Excel files.

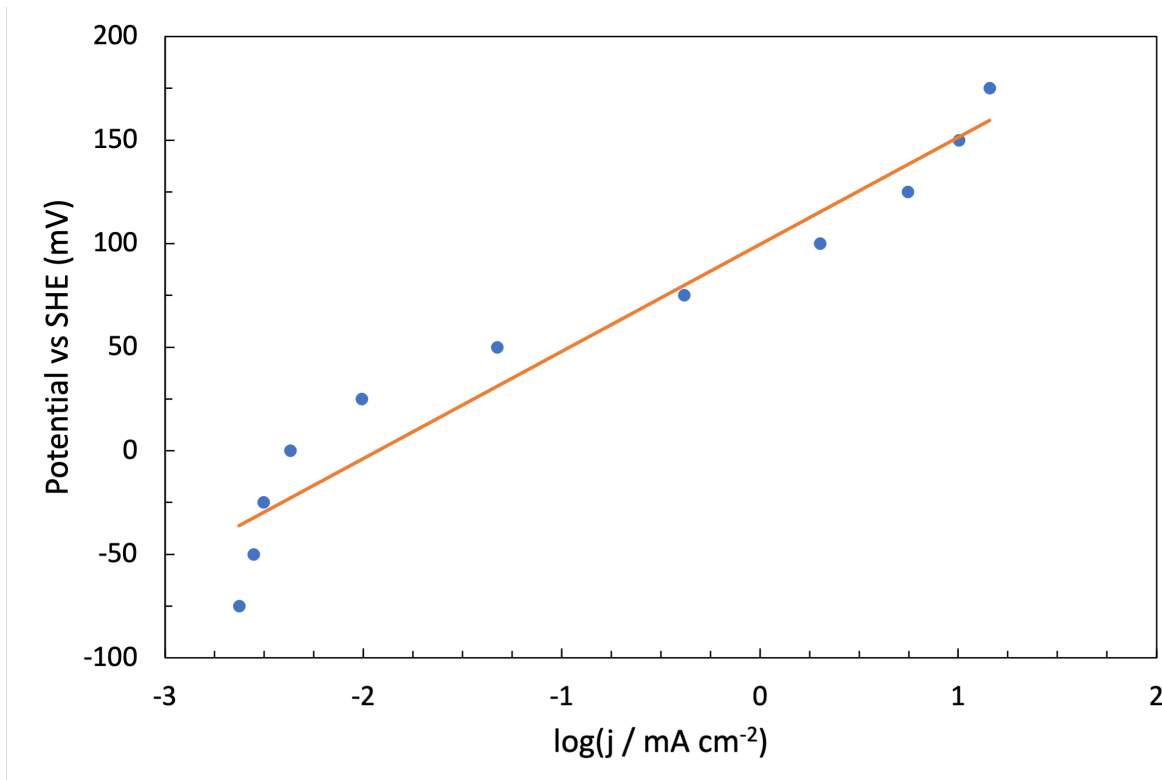


Figure 8. Tafel plot for the HER over a Pt electrode in 0.1 M H₂SO₄. The potentials (in V) were selected on the basis of preceding cyclic voltammetry experiments to surround the foot of the catalytic wave in 25 mV intervals. The logarithmic current densities were calculated from the average current measured at each potential in the last 30 s of a 100 s cyclic amperometry experiment conducted at a given potential, and normalized using the platinum electrode surface area of 0.0314 cm². Data analysis and linear regression was performed in Excel using the Solver function. A positive Tafel slope is observed: $m = 48 \text{ mV/dec}$ and $b = 101 \text{ mV}$ for a fit to $\eta = m \cdot \log(j) + b$.

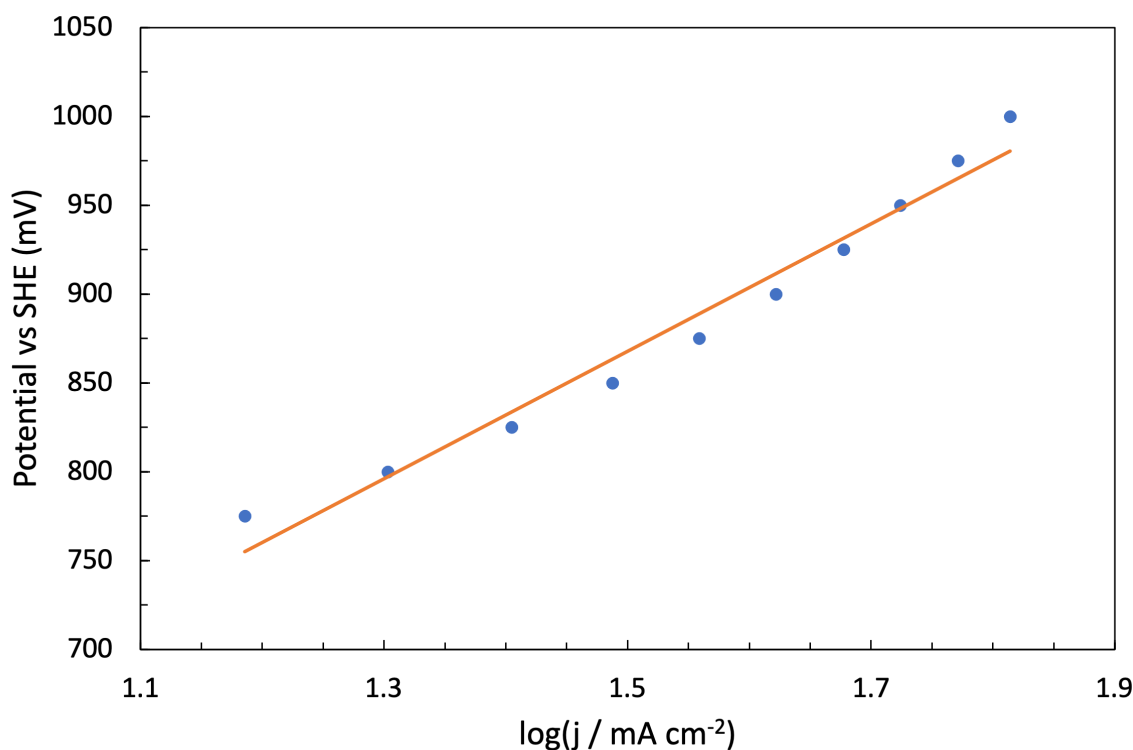


Figure 9. Tafel plot for the HER over a Sn electrode in 0.1 M H₂SO₄. The potentials (in V) were selected on the basis of preceding cyclic voltammetry experiments to surround the foot of the catalytic wave in 25 mV intervals. The logarithmic current densities were calculated from the average current measured at each potential in the last 30 s of a 100 s cyclic amperometry experiment conducted at a given potential, and normalized using the tin electrode surface area of 0.48 cm². Data analysis and linear regression was performed in Excel using the Solver function. A positive Tafel slope is observed: $m = 359 \text{ mV/dec}$ and $b = 330 \text{ mV}$ for a fit to $\eta = m \cdot \log(j) + b$.

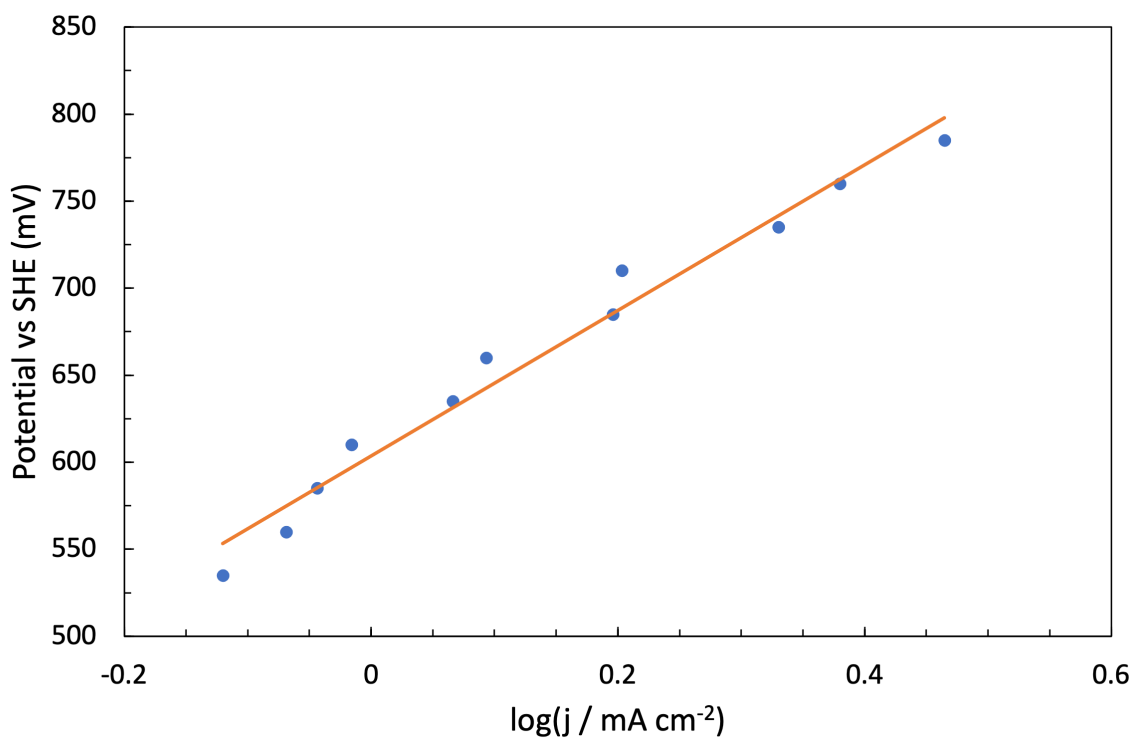


Figure 10. Tafel plot for the HER over a Ti electrode in 0.1 M H₂SO₄. The potentials (in V) were selected on the basis of preceding cyclic voltammetry experiments to surround the foot of the catalytic wave in 25 mV intervals. The logarithmic current densities were calculated from the average current measured at each potential in the last 30 s of a 100 s cyclic amperometry experiment conducted at a given potential, and normalized using the platinum electrode surface area of 0.63 cm². Data analysis and linear regression was performed in Excel using the Solver function. A positive Tafel slope is observed: $m = 402 \text{ mV/dec}$ and $b = 608 \text{ mV}$ for a fit to $\eta = m \cdot \log(j) + b$.

The Tafel slopes for platinum and tin are different. In particular, the respective slopes are 48 mV/log(j) and 359 mV/log(j). Comparing these values with the predicted Tafel slopes in the introduction reveals that platinum most likely proceeds via a V-T mechanism and thus exhibits an acid concentration dependence of 2, while tin most likely proceeds via a V-H mechanism and thus exhibits an acid concentration dependence of 1.

On rate laws, the above concentration dependence and Wuttig⁷ imply that

$$R_{\text{Pt}} = k_1 [\text{H}_3\text{O}^+]^2 e^{-\beta \eta F/RT} \quad (10)$$

and

$$R_{\text{Sn}} = k_2 [\text{H}_3\text{O}^+] e^{-\beta \eta F/RT} \quad (11)$$

Lastly, it follows from the CV data (Figures 2-7) that the optimal binding energetics of the hydride intermediate should preferably be bound neither too tightly nor too loosely. This results in a “volcano plot” of transition metals, as seen in the lab manual⁹.

Conclusion

In this experiment, the onset potential was determined for each metal by finding the foot of the catalytic wave in the CV diagrams. This illustrated that Pt was the most active electrocatalyst, followed by Ti and then Sn. The foot of the catalytic wave was also used to locate points for use in chronoamperometry with the goal of constructing a Tafel plot. Said plot enabled the determination of which reaction mechanism took place over each metal (specifically Pt and Sn). In particular, it was determined that Pt makes use of the V-T mechanism while Sn makes use of the V-H mechanism. Overall, the data suggested the strong role of metal-hydride binding energetics in determining catalytic efficiency and activity.

Throughout the experiment, several sources of error likely affected results. First off, corrosion and fragmentation of the tin electrode likely drastically affected its electrochemistry. In particular, some electrons likely went toward reducing the tin oxides created on the positive sweeps, increasing the measured current. This would have also lowered the Faradaic efficiency from 100%, affecting some later calculations. Additionally, both the platinum and titanium electrodes likely undergo mild oxidation and corrosion, too, hence the requisite cleaning after each scan. Thus, the surface area is likely not constant throughout the reaction but would shrink, slightly raising the current density in later cycles. Moreover, normalization would need to be conducted in a more sophisticated manner. Furthermore, the tin and titanium electrodes were made in-house and not of the same professional caliber as the platinum electrode, so their more rudimentary form likely made the data collected on them generally less accurate as well. One last bit of experimental error is the aforementioned failure to stir the reaction during the platinum CA experiment likely made that data less than perfect, and extra cleaning of the cells between experiments would have made the data more accurate as well. On the analytical side, the models used generally gave interpretations of the data consistent with the theory. However, one particular place where they may be incomplete is indicated by the smoothness of the hypothetical curve connecting the data points in Figures 2-5 and 3-6. That the curve would be so smooth is highly unlikely statistically, and likely suggests the presence of a higher level chemical process containing more relevant information that the simplistic linear regression used does not capture.

Altogether, the data herein provides insight into the catalytic mechanism of hydrogen evolution over potential electrocatalysts, confirming the strong ability of one particular material (platinum) to catalyze said reaction and making it easier to design future experiments regarding this critical clean energy tool.

References

- (1) Huber, K. P.; Herzberg, G. H. In *NIST Chemistry WebBook, NIST Standard Reference Database Number 69*, Linstrom, P. J., Mallard, W. G., Eds., <https://doi.org/10.18434/T4D303>; National Institute of Standards and Technology: Gaithersburg MD, 20899; Chapter Constants of Diatomic Molecules.
- (2) McNaught, I. J. The Electronic Spectrum of Iodine Revisited. *J. Chem. Educ.* **1980**, *57*, 101–105.
- (3) Lant, H. Electronic Spectroscopy: Absorption Spectra of Molecular Iodine in the Gas Phase, Rev. 1-21-23, 2023.
- (4) Verma, R. D. Ultraviolet Resonance Spectrum of the Iodine Molecule. *J. Chem. Phys.* **1960**, *32*, 738–749.
- (5) Saiz-Lopez, A.; Saunders, R. W.; Joseph, D. M.; Ashworth, S. H.; Plane, J. M. C. Absolute absorption cross-section and photolysis rate of I_2 . *Atmos. Chem. Phys.* **2004**, *4*, 1443–1450.
- (6) Seh, Z. W.; Kibsgaard, J.; Dickens, C. F.; Nørskov, J. C. J. K.; Jaramillo, T. F. Combining theory and experiment in electrocatalysis: Insights into materials design. *Science* **2017**, *355*, eaad4998.
- (7) Wuttig, A. Electrochemistry, Video lecture, Chicago, IL: University of Chicago, 2023.
- (8) Laursen, A. B.; Varela, A. S.; Dionigi, F.; Fanchiu, H.; Miller, C.; Trinhammer, O. L.; Rossmeisl, J.; Dahl, S. Electrochemical Hydrogen Evolution: Sabatier’s Principle and the Volcano Plot. *J. Chem. Educ.* **2012**, *89*, 1595–1599.
- (9) Wuttig, A.; Lant, H. Electrokinetics: Mechanism of Hydrogen Evolution on Catalytic Transition and Late Metal Electrodes, 2023.
- (10) Pourbaix, M., *Atlas of Electrochemical Equilibria in Aqueous Solutions*; National Association of Corrosion Engineers: 1440 South Creek Drive, Houston, Texas 77084, 1974.
- (11) Connor, P.; Schuch, J.; Kaiser, B.; Jaegermann, W. The Determination of Electrochemical Active Surface Area and Specific Capacity Revisited for the System MnO_x as an Oxygen Evolution Catalyst. *Z. Phys. Chem.* **2020**, *234*, 979–994.